3-D IMAGING OF ROOT ARCHITECTURE USING MULTICHANNEL GPR

MULTICHANNEL 3-D GROUND-PENETRATING RADAR (GPR) IMAGING OF TREE ROOT ARCHITECTURE FOR BIOMASS ESTIMATION

BY

DOUGLAS BLOMFIELD B.Sc. (Hons)

A Thesis Submitted to the School of Graduate Studies in Partial Fulfillment of the Requirements for the Degree of Masters of Science

McMaster University

MASTER OF SCIENCE (2017)	MCMASTER UNIVERSITY
Geography and Earth Sciences	Hamilton, Ontario
TITLE:	**MULTICHANNEL 3-D GROUND-PENETRATING RADAR (GPR) IMAGING OF TREE ROOT ARCHITECTURE FOR BIOMASS ESTIMATION**
AUTHOR:	Douglas Blomfield, B.Sc (Hons)
	(McMaster University, Hamilton, 2014)
SUPERVISOR	Dr. Joseph I. Boyce
NUMBER OF PAGES	xiii, 73

LAY ABSTRACT

Forests play an important role in the global carbon cycle by removing carbon from the Earth's atmosphere and storing it in tree tissues as biomass. Estimation of the amount of biomass and carbon stored in forests is critical to predictive climate change models, and increasingly employs remote sensing methods to detect both the above ground biomass (e.g. leaves, tree branches) and the belowground carbon in the tree root system. Measurement of the belowground biomass is most difficult, as it cannot be directly observed without destructive excavation of the tree root system.

This study investigated the application of new technology, multi-channel ground penetrating radar (GPR), for mapping tree root systems. The GPR system (IDS Hi-BrigHT) employs 'swath mapping' using high frequency pulsed radio waves and multiple transmitting and receiving antennas to produce detailed maps of roots structure. The GPR capabilities were evaluated at a test site at the Turkey Point Flux Station (TPFS) in southern Ontario. The root system of a juvenile white pine tree (20-30 cm diameter) was swath mapped over a 25-m^2 area with a line spacing of 2 cm. The GPR data were processed to produce a 3-dimensional radar volume, which can be 'sliced' in various orientations to reveal the root structure. The time slice maps show that roots as small as 1-cm can be detected and roots larger than 3 cm in diameter can be mapped as continuous root segments.

ABSTRACT

Root biomass accounts for about 25% of the carbon storage in mid-latitude forests. Estimation of root biomass for carbon cycling studies requires either direct measurement by excavation of root systems, or remote measurement using ground penetrating radar (GPR) or other geophysical methods. This study evaluated the ability of a 2-GHz multi-channel GPR system (IDS Hi-BrigHT) to detect and map white pine roots in managed forest near Turkey Point, southern Ontario. The GPR system employed eight dual-polarized antenna pairs separated at 10 cm intervals. GPR data were acquired as overlapping swaths (2 cm line spacing, 0.4 cm inline) across a 25-m^2 test site (TP74-R) containing a juvenile white pine tree. Radargrams were processed to full 3-D radar volumes for time slicing and interpretation of root architecture and comparison with the excavated root network.

Radargram signal processing was successful in suppressing airwave and other background noise and improved the detection of root diffractions on radargrams. The majority of roots were found in the rooting zone at a depth of 5-40 cm. Roots as small as 0.5 cm were detected with the 2-GHz frequency, but many roots <1.5 cm diameter could not be detected as continuous root structures. Root detection was strongly dependent on root orientation; large, coarse roots (>3-5 cm) were imaged as continuous root segments when oriented perpendicular to GPR profiles. Roots intersecting GPR profiles at angles <30-45 degrees were either imaged incompletely or not detected on radargrams. The highest rate of root detection was achieved with horizontally polarized (HH) antennas (dipole axis parallel with the root structures). Isosurface root models constructed from the Hilbert-transformed radargrams allowed mapping of the 3-D dimensional root architecture for large (> 3-5 cm diameter) roots. Isosurface models provide a means for estimating the coarse root volume for large roots and could be employed in future work to monitor temporal changes in root biomass by repeat survey at the same measurement site.

Keywords: 3-D multi-channel GPR, dual polarization, tree roots, root detection

ACKNOWLEDGEMENTS

I would first like to take the time to thank Dr. Joseph Boyce. He was instrumental throughout the entire process and always gave support when needed. He was a patient and thorough teacher and I am very thankful to have had the opportunity to work with him.

I also want to thank my family. Mom and Dad, thanks for always being available to talk to even if you didn't always understand the material. Pam, thanks for helping me through the rough spots; couldn't have done it without you. Thank you Alex for always pushing me when I needed it and not letting me give up on this project. I am forever thankful for your support.

Thank you to my two helpers, Iwona and Tristan, without whom I would still be out at the mosquito infested study site collecting data. You guys kept me sane out there and I appreciated it more than you know. Thanks to my office mates Anya, Bobby, Cam, Chelsi, Corey, Jeremy, Nick, Majed, Ty, Shawn, and Winnie. You guys always made work (and lunch) more enjoyable.

Thank you to IDS and Alex Novo for training us to use the Hi-BrigHT and always being able to answer any questions we had. Another big thanks goes out to Dean Goodman, who would always get back to my e-mails even in the middle of the night.

The research project was supported through Natural Sciences and Research Council of Canada (NSERC) Strategic Project and Discovery Grants to J. Boyce and M.A. Arain. We thank colleagues at the Ontario Ministry of the Environment for access to the field site and in-kind support of research work at the Turkey Point Flux Station.

TABLE OF CONTENTS

LIST OF FIGURES

Chapter 1:

Chapter 2:

resolution shown by green box in lower right survey grid. (B) Vectorized root network for 25-m^2 area shown above.

Figure 2.3: (A) Monostatic GPR antenna. (B) Antenna footprint.

Figure 2.4: (A) Broadside antenna configuration. Electrical vector (E) contained within horizontal polarization plane (EH or HH mode). (B) End-fire antenna orientation, with antennas parallel to profile and electrical vector (E) in the vertical polarization plane (EV or VV mode). From Baker and Jol (2007).

Figure 2.5: (A) Vertical resolution as a function of antenna centre frequency. (B) Nyquist line interval for centre frequency of 2-GHz. Note the Nyquist sampling interval is approximately 1.75 cm. (C) Variation in GPR beam foot print with depth. A is major axis and B is and semi-major axis (see Fig. 2.3B).

Figure 2.6: Hi-BrigHT multichannel GPR system. The system includes a 16-channel dual-polarized antenna array mounted on a two-wheel trolley. Inline sampling position is recorded by an odometer wheel.

Figure 2.7: Schematic showing internal configuration of dual polarized antenna arrays in Hi-BrigHT system. HH= horizontal polarization. VV = vertical polarization. Note antenna elements are numbered from right to left.

Figure 2.8: Schematic showing the swathing pattern employed at both test sites to acquire overlapping swaths (2-cm line spacing) with the Hi-BrigHT antenna.

Figure 2.9: Survey grid showing survey line paths at site TPFS-74-R. Line spacing is 2 cm.

Figure 2.10: Schematic showing GPR processing steps in GPR-SLICE software.

Chapter 3:

LIST OF TABLES

Chapter 2

LIST OF ALL ABBREVIATIONS AND SYMBOLS

Abbreviation or Symbol	Explanation
GPR	Ground Penetrating Radar
TPFS	Turkey Point Flux Station
VV	Vertically polarized antennas
HH	Horizontally polarized antennas
IDW	Inverse distance weighting
TP74	Turkey Point 74; a white pine plantation planted in 1974
GHz	Gigahertz
MHz	Megahertz
Tx	Transmitter
Rx	Receiver

Chapter 1: Introduction

1.1 Background

Forests are important carbon sinks, accounting for about $1.1x10^3$ petagrams of carbon globally (Dixon et al., 1994). Tree roots account for about 20-30% of the total carbon sequestered in forests, but this component is the most difficult to quantify, as it is belowground (Piechl and Arain, 2006; Borden et al., 2014). Conventionally, the estimation of tree root biomass requires the excavation of tree root networks and destructive harvesting of roots. The harvested root biomass is then employed to develop allometric equations that relate the tree diameter at breast height (DBH) to total root biomass (Piechl and Arain, 2006). This approach is both time-consuming and destructive to the forest and the derived allometric equations are site and species specific.

An alternate approach to destructive harvesting and allometric biomass estimation is to map root networks remotely using non-invasive geophysical methods such as ground-penetrating radar (GPR) (Hruska et al., 1999; Al Hagrey, 2008; Molon et al., 2017). GPR is a non-invasive geophysical method for imaging the shallow subsurface and detecting buried objects (Isaac et al., 2013). GPR systems measure the two-way travel time of pulsed high-frequency (0.1-2 GHz) radarwaves reflected at boundaries with contrasting relative permittivity (Fig 1.1). The arrival of the reflected radar impulse is recorded by a second receiving antenna and the depth of the target is determined from the two-way travel time and radarwave velocity (Annan, 2003). Typically, low frequency GPR systems (<200 MHz) enable deeper penetration and lower resolution while mid- to high-frequency systems have high resolution but reduced penetration (Barton and Montagu, 2004).

Roots can be normally detected with GPR when there is a strong contrast in the moisture content of the soil and root tissues, and where soil permittivity and conductivity are conducive to radarwave propagation. The root/soil permittivity contrast is generally greatest in well-drained, sandy soils (Hirano et al., 2009) and roots can be detected as well-defined hyperbolic diffraction events on radargrams (Fig. 1.1). Root detection requires the use of high-frequency (0.5-2 GHz) GPR antennas, as the vertical and horizontal resolution is a function of the signal wavelength, target depth and the soil electromagnetic properties (see section 2.1).

1.1.1 Previous work

A number of previous studies have demonstrated the application of GPR to root detection and belowground biomass estimation (Guo et al., 2013). Hruska et al. (1999) demonstrated that coarse roots (> 3 cm diameter) could be mapped with 450-MHz GPR and Butnor et al. (2001) evaluated 450 and 1500 MHz GPR antennas for mapping roots under a variety of soil conditions. In the latter study, roots 0.5-6.5 cm in diameter were detected, but the authors noted that the root detection was highly site-specific and dependent on soil type, moisture content and root orientation. Barton et al. (2004) tested the ability of 500, 800 and 100 MHz GPR to detect reburied roots in a 25-m^2 test pit. They were able to detect roots as small as 1 cm diameter and demonstrated a method for predicting root diameter from reflection amplitudes using regression analysis. Bassuk et al. (2011) employed 900 MHz antenna to identify coarse roots buried under concrete. Their study showed that the GPR could reliably predict coarse roots but individual root detection was more difficult. Cui et al (2011) demonstrated that roots > 0.5 cm diameter could be imaged with a 2 GHz GPR system. They encountered problems when the system attempted to image the finer roots (< 0.5 cm) as well closely-spaced roots.

In addition to root detection and mapping, several studies have evaluated GPR as a tool for quantifying belowground root biomass. Most of these studies have estimated biomass using indices derived from radargram amplitudes or measurement of the radar pulse shape (see Fig. 1.2). Butnor et al (2001) employed image analysis software to determine the peak area amplitude area of root diffraction events (p; Fig. 1.2B) and found a correlation coefficient with root diameter of r = 0.46-0.55. Dannoura et al., (2008) and Hirano et al. (2009) obtained better correlations (r=0.64-0.83) using pixels within a threshold range regressed on root diameter. Other studies have employed waveform parameters to estimate root diameter (Fig. 2.1C), which have yielded a better correlation with root diameter than reflected wave amplitude (Barton et al., 2004; Cui et al. 2011). Molon et al. (2017) employed a deterministic approach, which estimated the root volume directly from isosurfaces calculated on Hilbert-transformed 3-D GPR volumes using the marching cubes algorithm.

1.1.2 Limitations of GPR

GPR methods can detect roots under favourable soil conditions but there are several factors which limit its application in root mapping and biomass estimation (Cui et al., 2011; Guo et al. 2013). Root detection is strongly controlled by the contrast in soil and root moisture content. Hirano et al. (2009) found that roots with less than 20% water content and < 1.9 cm in diameter could not be detected with 900 MHz GPR. This same study found that closely-spaced roots would often be detected as one large root (Hirano et al., 2009).

As demonstrated by Butnor et al. (2001), root detection is highly site specific and dependent on soil properties. Conductive, clay-rich soils strongly limit radarwave penetration and are not well-suited to GPR studies; root detection is limited to areas with well-drained, sandy soils. The presence of heterogeneity and soil stratification can also create significant clutter on radargrams, making it difficult to detect root diffractions. For example, coarse-textured soils containing pebble or boulder-sized clasts can produce false root detections as can the presence of or organic matter (e.g. logs, plant debris)(Molon et al., 2017). These heterogeneities can make it difficult to discern noise from root diffractions on radargrams.

The orientation of roots also exerts a strong control on root detection (Tanikawa et al., 2013). For typical broad-side antenna set-up (see section 2.2.1), roots that are perpendicular (90 degrees) to the survey profile produce the largest amplitude reflections. When the angle between the root and GPR profile is less than 45 degrees or greater than 135 degrees, the diffraction amplitude is reduced and detection becomes increasingly difficult (Tanikawa et al., 2013). Tanikawa (2013) advocated the use of an orthogonal survey grid, as this would ensure that most roots were within the preferred orientation for detection. The detection of closely-spaced roots, and roots that are stacked on top of each other can also be problematic due to overlap and interference of root diffractions, which makes it difficult to pinpoint the exact location of roots (Barton and Montagu, 2004).

Due to the small diameter of tree roots, antennas with a centre frequency of 500 - 2000 MHz are required for detection (Barton and Montagu, 2004; Cui et al., 2013). However, site surface conditions can hinder the propagation of the high-frequency radarwaves, particularly if there is heavy ground organic litter. Prior to survey work, surface litter and foliage should be cleared (Butnor et al., 2005). The relative permittivity and conductivity of soils also plays a key factor in tree root detection. Generally, the permittivity of dry sandy soils ranges from 3-5, whereas freshwater typically has a conductivity of 80-81. This means that even a small increase in water content can cause a large increase in permittivity. This can cause radar signals to weaken and subsequently make it difficult to delineate tree roots under wet conditions (Conyers, 2004). Root detection is also problematic in lossy conductive soils with significant clay or soluble salt content. The more electrically conductive the soil is, the greater the radarwave will be attenuated with propagation depth (Guo et al., 2012). Larger roots are more easily detected using GPR but even large diameter roots may be difficult to detect at depth, due to attenuation losses (Butnor et al., 2001). In fact, larger roots are more affected by depth attenuation than smaller diameter roots (Hirano et al., 2012). Cui et al. (2011) noted that most GPR biomass studies did not account for the attenuation of spherical spreading of the radar wave with depth, which led to the incorrect processing of radargrams and in turn, an inaccurate estimation of biomass.

The positioning of antennas and survey navigation are critical for high-resolution GPR acquisition (Grasmueck and Novo, 2016). As a GPR antenna is moved across the surface topography the antenna motions produce variations in angle of the transmit beam relative to the ground surface, which can lead to misplacement of root diffraction events on radargrams. These effects can be minimized by measuring the antenna motions (i.e. pitch, roll and yaw) during the survey and by applying a correction for beam angle during post-processing (e.g. Molon, 2012; Goodman and Piro, 2013). Molon (2012) employed an accelerometer and tilt measuring device attached to a 1-GHz GPR system to measure and correct for microtopographic effects. She showed that small variations in surface relief can produce substantial errors in radargrams and that corrections applied to the beam vector can increase the coherency of 2-D radagrams and 3-D radar volumes. At present, commercially available GPR systems, including multi-channel systems, do not incorporate accelerometers or other devices for measuring the antenna orientation. In conventional GPR processing, corrections for surface topographic relief typically involve a simple a trace-by-trace bulk time shifts account for time delays due to surface relief. Goodman et al. (2006) demonstrate a method for calculating corrections for the beam angle using the measured surface topography.

1.2 Objectives

The estimation of belowground root biomass is fundamental component of modelling of global carbon fluxes (Arain and Restrepo-Coupe, 2005; Stover et al., 2007). In Canada, knowledge of carbon sequestration in forests is also critical to development of afforestation programs being implemented as carbon reduction measures (e.g. Piechl and Arain, 2006). GPR and other geophysical methods can provide an alternate method for root biomass estimation and, as reviewed in the previous section, quantitative estimates of root biomass can be achieved (Borden et al., 2015, Molon et al., 2017). However, most work to date has emphasized the estimation of root biomass in *2-D radar profiles* using amplitude-derived parameters to measure root diameter and volume (e.g. Fig. 1.2)(Guo et al., 2013); few systematic attempts have been made to map the 3-D root architecture using *full 3-D ground penetrating radar* (Grasmueck et al., 2005; Zhu et al. 2013; Grasmueck and Novo, 2016; Molon et al., 2017). This contrasts with other areas of GPR application (e.g. engineering, archaeology) where full 3-D GPR imaging is now routinely employed for detecting and mapping buried structures (e.g. rebar, buried architectural features; Grasmueck et al., 2016). Further work is now needed to investigate the potential of 3-D multi-channel GPR as a tool for root detection and biomass estimation.

The overall objective of this thesis was to evaluate the use of multi-channel GPR methods for detecting and mapping 3-D root networks at the Turkey Point managed pine forest in southern Ontario (Fig. 1.3). The specific thesis objectives were:

1. to acquire a high-resolution multichannel GPR survey of two forest test plots under controlled survey conditions,
2. to determine the vertical and horizontal resolution that can be achieved with a 2-GHz multi-channel GPR system and to evaluate methods for interpolating 2-D profiles to 3-D radar volumes

3. to determine the survey positioning and instrument navigation requirements for high-resolution mapping of roots using a guidance rail system
4. to evaluate the potential for mapping of root networks and root architecture in plan view (2-D mapping) and in full 3-D radar volumes

1.3 Thesis format and contributions

This dissertation is formatted as a conventional thesis with five separate chapters. Chapter 1 introduces the research problem and provides an overview of previous work that has employed GPR to detect tree roots. Chapter 2 documents the study site and research methods, including a detailed discussion of the GPR processing methods. The thesis results are presented in Chapter 3 including the outcomes of radargram processing, 3-D radar volume generation and root network mapping. Chapter 4 provides a discussion of the research results, including an analysis of sources of error and evaluation of the benefits and potential for biomass studies. Chapter 5 summarizes the thesis results and outlines some areas for potential future research work, including discussion of improvements to the multichannel data acquisition and processing.

D. Blomfield was responsible for GPR field data collection, data processing, thesis preparation and production of figures and tables. J. Boyce supervised the research and provided technical review and thesis editing. Undergraduate students T. Goodwill and I. Widurska assisted with GPR field data collection and GPS survey of field sites in 2015 and C. Dimaria assisted with data processing.

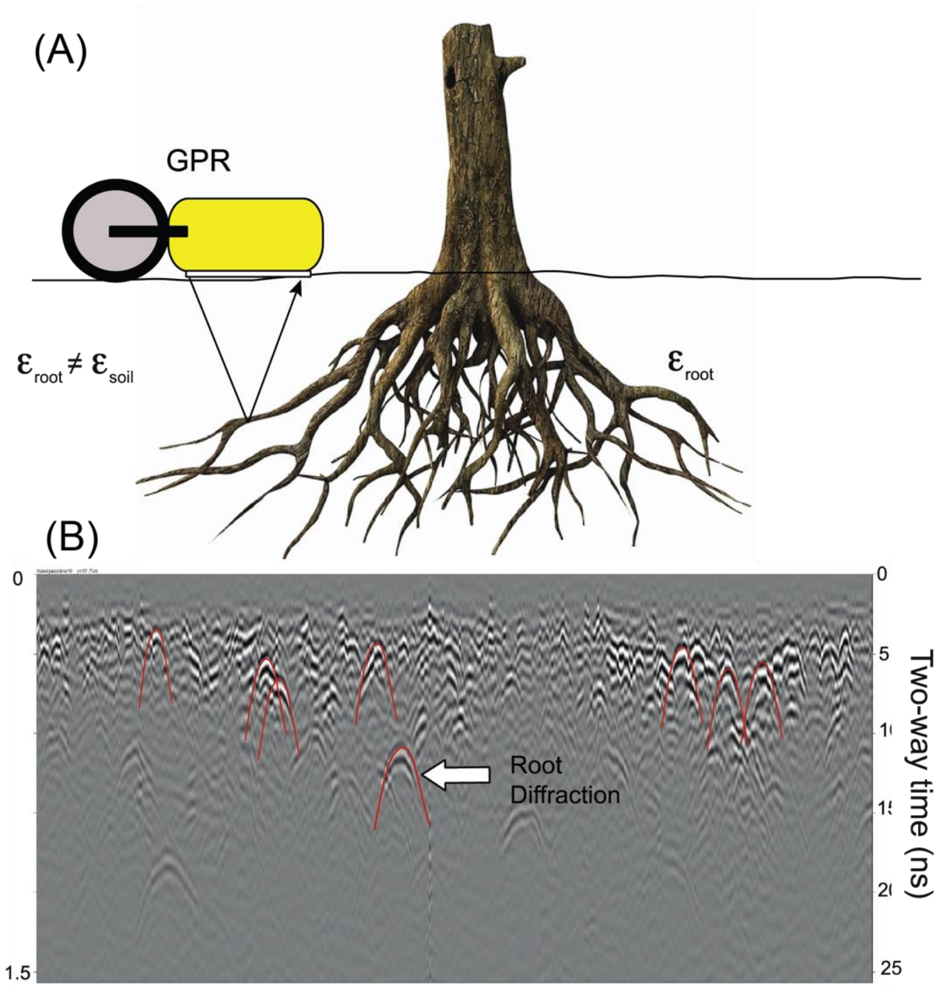

Figure 1.1: (A) Principle of ground-penetrating radar imaging. (B) Example radargram showing root diffraction events. Diffractions are indicated by inverted "U" hyperbolic reflections. The apex of the hyperbola indicates the root top center location.

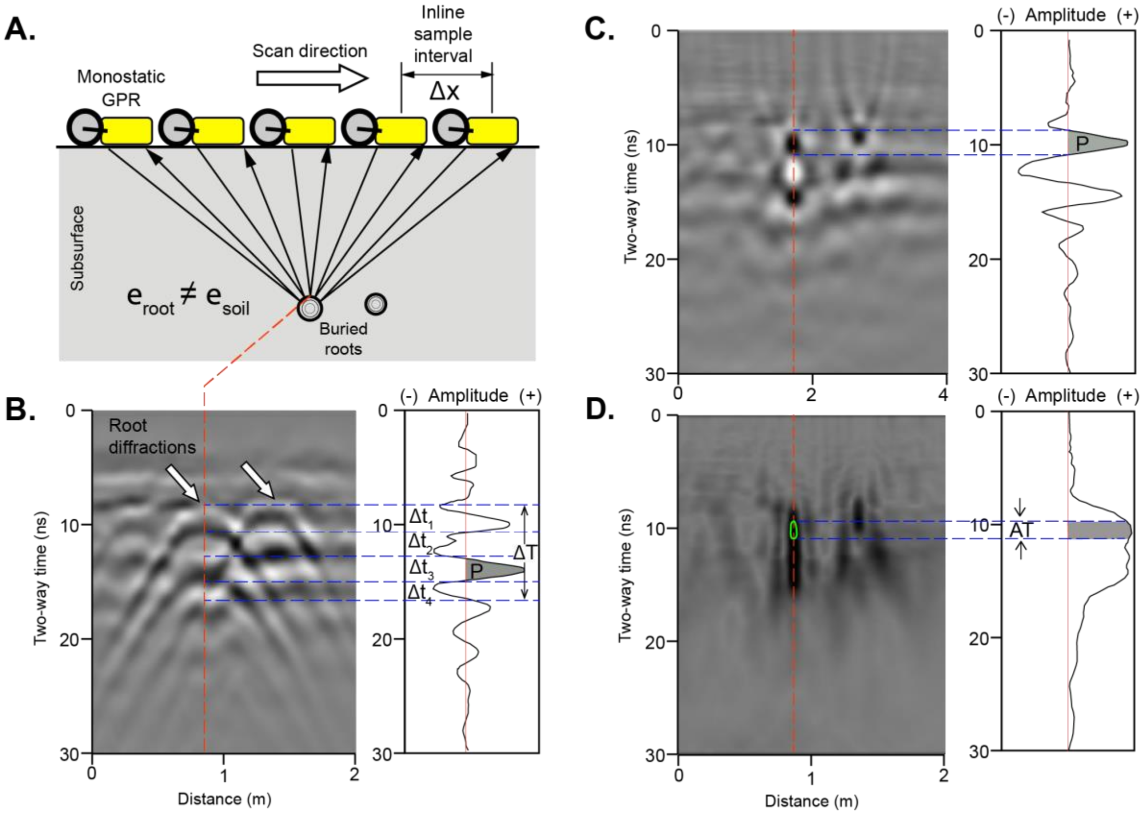

Figure 1.2: (A) Variation in reflection path length and two-way travel time as GPR antenna moves across two buried roots. (B) Radargram showing root diffractions with single GPR trace on right. Various GPR waveform indices (ΔT, Δt1 – Δt4, P = peak area amplitude) employed in previous studies for estimation of root diameter also shown (Barton and Montagu, 2004; Butnor et al., 2005; Guo et al., 2013a, b; Zhu et al., 2014). (C) Migrated radargram. Single migrated trace with peak amplitude area indicated for first cycle in root reflection shown on right. (D) Hilbert-transformed radargram. Isosurface calculated for using amplitude threshold (AT) of 85% shown as green isoline on radargram. Note Hilbert transform collapses multiple wavelet cycles to a single high amplitude focus. Modified from Molon et al. (2017).

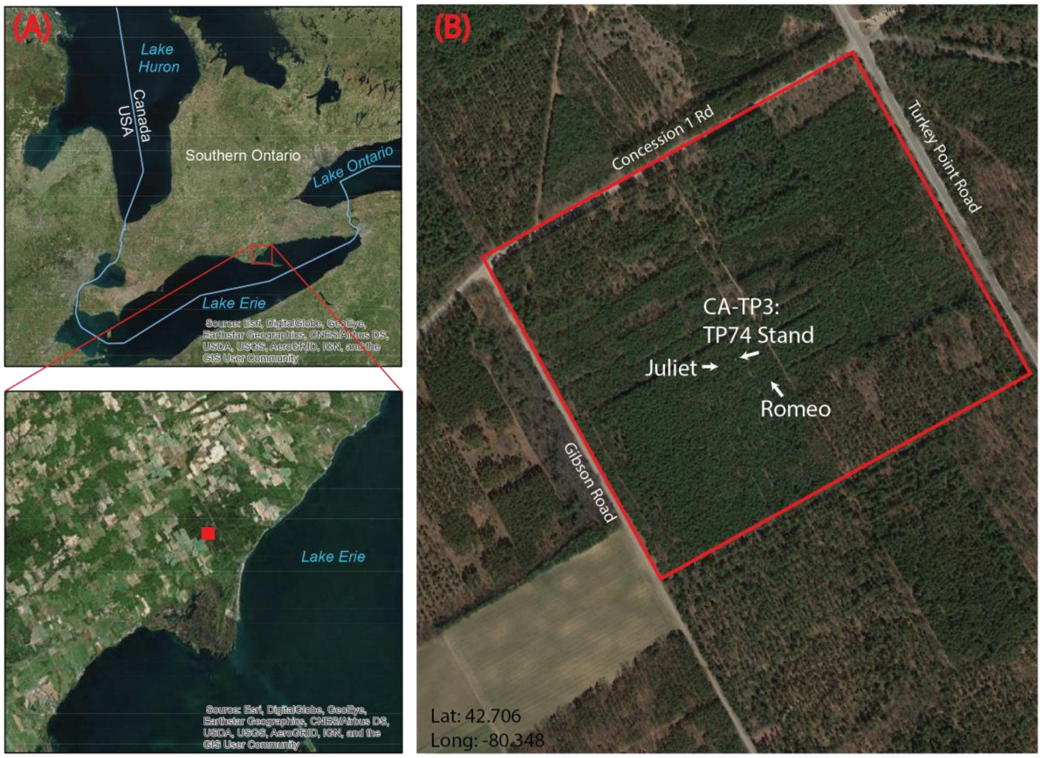

Source: Esri, DigitalGlobe, GeoEye, Earthstar Geographics, CNES/Airbus DS, USDA, USGS, AeroGRID, IGN, and the GIS User Community

Source: Esri, DigitalGlobe, GeoEye, Earthstar Geographics, CNES/Airbus DS, USDA, USGS, AeroGRID, IGN, and the GIS User Community

Figure 1.3: (A). Location of study area in southern Ontario. (B) Aerial photo showing two GPR test sites (Romeo, Juliet) located in Turkey Point Flux Station (TPFS) white pine plantation.

Chapter 2: Study Area and Methods

2.1 Study Area

The study was conducted at the Turkey Point Flux Station (TPFS), a managed forest located about 20 km southwest of the town of Simcoe, Ontario (Fig. 1.3). The TPFS is a carbon flux monitoring site and is part of the FLUXNET global monitoring network (Arain and Restrepo, 2005; Peichl et al., 2010). The forest contains two separate white pine stands planted in 1939 and 1974, which are currently managed by the Ontario Ministry of Natural Resources (Fig. 1.3). GPR studies were conducted at two sites within the 1974 stand (TP74). The forest is dominated by eastern white pine (*Pinus strobus L.*) but also contains other species including balsam, fir and other native Carolinian species. The ground cover is made up of mosses (*Phlox subulata*), poison ivy (*Rhus radicans*) and bracken fern, Canada mayflower (*Maianthemum canadense*) and allegheny raspberry (*Rubus allegheniensis*) (Peichl and Arain, 2006).

The TPFS is located on a broad sand plain deposited during a higher-level phase of postglacial Lake Erie. The soil is a very fine grey-brown luvisol with a sandy texture. It has an average composition of 98% sand, 1% silt and 1% clay. The bulk density of the upper 10 cm is 1.35 gcm^{-3} (Peichl and Arain, 2006; Peichl et al., 2009) and is well-drained. The area has a mean annual temperature of 7.8 °C and an annual precipitation of 1010 mm (Molon et al., 2012).

2.1.1 Test Sites

Two juvenile white pine trees were selected as survey sites (TP74-R, TP74-J; Fig. 2.1). Sites were selected where the forest floor was relatively flat and where there were no neighboring trees within a 4-metre radius to allow for unobstructed survey of a 5 x 5 m area around each tree. The pine tree at site TP74-R had a diameter at breast height (DBH) of 27 cm and at site TP74-J of 24 cm. This thesis documents the results of multi-channel GPR survey at the first test site, TP74-R. Air-spading and root exposure was not conducted at the second site (TP74-J) as it is being preserved for use as a long-term biomass monitoring site. The GPR results from TP74-J will reported in a separate study.

The survey navigation at TP74-R employed a guide rail system and use of GPR survey wheel odometer. A 6 x 6 m wooden box was constructed around the tree using 2x10” boards laid on edge and fastened at the corners with metal brackets (Fig. 2.1). The box perimeter was marked at 1-cm intervals to provide survey reference marks for positioning of a GPR guide rail system. This guide rail system consisted of a 6.2 m wooden rail that spanned the width of the 6 x 6 m survey box (Figs. 2.1, 2.2). The guide rail was positioned on the survey box perimeter using alignment marks, which allowed for positioning of the antenna system with an estimated cross-line positional accuracy of about 0.5 cm. A 0.5 m setback was required along the inner edge of the box to allow for positioning of the antenna odometer wheel, providing a working survey area of 25-m^2 (Fig. 2.2). Prior to survey work, the surface litter within the box was removed and the soil surface raked and tamped to provide an even flat surface for unobstructed movement of the GPR antenna. When the study areas were not being surveyed a waterproof tarp was placed over the study sites to prevent water from permeating into the soil which would interfere with the detection of the roots.

Following the survey at site TP74-R, the tree was harvested and the root system was exposed by air-spading to a depth of 30 cm (Fig. 2.2). The air spading system employs a high-pressure air stream to clear the area of surface debris and soil, but does not harm plant roots, buried cables, or other buried objects. A reference grid was then placed across the exposed roots by anchoring cord to the box perimeter at 0.5 cm intervals (Fig. 2.2). The roots were then photographed overhead using a 20-megapixel digital camera positioned on a step ladder to provide a reference image for comparison with the GPR images. The photograph was orthorectified and georeferenced to the survey grid using GlobalMapper software (Fig. 2.2).

2.2 GPR Principles

Ground penetrating radar (GPR) or ‘georadar’ has been in use since the mid-1970’s as a method for profiling the shallow subsurface and is now employed widely in engineering, geoscience and archaeological applications (Davis and Annan, 1989; Annan, 2003; Baker and Jol, 2007). GPR systems measure the travel time of high-frequency radarwaves propagated into the subsurface and reflected at boundaries where the relative permittivity (ε_r) is contrasting (Figs. 1.1).

The propagation of radarwaves is governed by the electromagnetic properties of the medium, including the electrical conductivity (σ), relative permittivity (ε_r), and relative magnetic permeability (μ_r). Permittivity can be defined as the ability of a substance to carry an electric charge when an electric field is present. The relative permittivity (dielectric constant) of a material ε_r is its permittivity measured as a ratio relative to vacuum:

$$\varepsilon_r = \frac{\varepsilon}{\varepsilon_0}$$

where ε_r is the permittivity of the material and $\varepsilon_0$is the permittivity of free space (8.854×10^{-12} Fm^{-1}) (Reynolds, 2012). Typical values for permittivity are shown in Table 1. The relative permittivity of air is ≈ 1 and fresh water is about 81. Because water has a very high value of ε_r, the relative permittivity of porous geological materials (e.g. sand) and wood are strongly dependent on their water content. Dry sand has a relative permittivity of about 3-6 compared with wet wood 10-30 (Reynolds, 2012). This fact explains why moist living roots are detectable in a dry sand soil and dead roots low moisture content are difficult to detect (Hirano et al., 2009; Molon et al., 2017).

Medium	Relative Permittivity (ε_r)	Velocity (m/ns)	Bulk Conductivity (mS/m)
Water (fresh)	81	0.033	0.5
Water (sea)	81 - 88	0.033	3000
Sand (dry)	3 - 6	0.122 – 0.173	10^{-4} - 1
Sand (wet)	10 - 32	0.053 – 0.095	0.1 - 10
Clay (dry)	2 - 5	0.134 – 0.212	2 - 100
Clay (wet)	8 - 40	0.047 – 0.106	20 - 1000
Wood (dry)	2 - 6	0.122 – 0.212	10^{-13} - 10^{-11}
Wood (wet)	10 - 30	0.055 – 0.95	0.1 - 1

Table 1: Relative permittivity, radarwave velocity and bulk conductivity values for selected materials. Note permittivity of dry sand and dry wood have similar ranges; detection of roots is highly dependent on moisture content of wood relative to soil volumetric water content.

Conductivity measures the ability of a material to transport charge in an electric field. Conductive materials (e.g. clays, salt water) strongly attenuate electromagnetic waves and are not conducive to GPR radarwave propagation. GPR penetration in clay soils with conductivities 20-1000 mSm^{-1} can be limited and are termed 'lossy' mediums. Penetration and radarwave propagation is optimal in dry sandy sediments which typically have low conductivity $\sigma = 10^{-4}$- 1 mSm^{-1}. Magnetic permeability is the ability of a substance to maintain a magnetic field.

The radarwave propagation velocity is dependent on electromagnetic properties as outlined above and is given by:

$$V_m = \frac{c}{\sqrt{\left(\frac{\varepsilon_r \mu_r}{2}\right)[(1+P^2)+1]}}$$

where P is the *loss factor* accounting for the energy loss in a dielectric medium:

$$P = \frac{\sigma}{\omega\varepsilon}$$

where σ is the bulk conductivity of the material, $\omega = 2\pi f$ is the angular frequency of the wave with f measured in Hz and ε is the dielectric permittivity of the material. In low-loss materials (e.g. most geologic materials) P ≈ 0 and the equation for radarwave velocity can be simplified to (Stover et al., 2007). The propagation velocity can be calculated using;

$$v = \frac{c}{\sqrt{\mathcal{E}_r}}$$

where *v* represents the propagation velocity, *c* represents the speed of light in a vacuum (3.0x10^8 ms^{-1}) and $\mathcal{E}_r$ is the relative permittivity (Annan, 2003; Reynolds, 2011). The radarwave velocity is commonly estimated by curve fitting to reflection hyperbolas on common-offset radargrams, or using semblance analysis and other techniques on common-midpoint, multi-channel radargrams.

Once the radarwave velocity is obtained, the target depth can be calculated as:

$$d = \frac{vt}{2}$$

where *d* is the depth to the reflector, *v* is the propagation velocity of the medium above the target and *t* is the two-way travel time of the radarwave.

The radarwave propagation in the subsurface is also a function of the design of the transmitting and receiving antennas. Most commercially available GPR systems employ bow-ties type antennas. The radiation pattern for bow-tie antenna can be approximated by an elliptical cone, diverging away from the antenna evenly as the wave propagates (Conyers and Goodman, 1997).

The travel time for a return signal from the transmitting antenna to the receiver decreases until it reaches a minimum value when the GPR unit is directly above the object it is imaging. This causes certain objects to be imaged before the system is directly above it. This creates a decreasing and increasing of travel time to the subsurface object which creates a hyperbolic pattern on the radar profile (Fig. 3.4). Tree roots appear in radargrams as hyperbolic events in which the apex of the hyperbola represents the actual location of the root.

The amplitude of the root diffraction on the radargram is dependent on the contrast in permittivity between the root and surrounding soil and also the attenuation characteristics of the soil (Guo et al., 2013). The permittivity contrast at the boundary and reflection strength can be estimated from the reflection coefficient R, (al Hagrey, 2007):

$$R = \frac{\sqrt{\varepsilon_1} - \sqrt{\varepsilon_2}}{\sqrt{\varepsilon_1} + \sqrt{\varepsilon_2}} = \frac{V_2 - V_1}{V_2 + V_1}$$

where ε_1 and ε_2 and V_1 and V_2 are the relative permittivities and radar wave velocities in the upper and lower medium respectively. The reflection coefficient can have positive or negative values ranging -1 to +1. R = 1 indicates complete reflection (no transmission through boundary) for the condition where $\varepsilon_1 > \varepsilon_2$ (velocity increase across interface) and R = -1 for complete reflection where $\varepsilon_1 < \varepsilon_2$ (velocity decrease across interface) (Hirano et al., 2009).

2.2.1 Antenna Polarization

A propagating electromagnetic wave (radar wave) is composed two orthogonal vector components, an electrical field vector (E_V) and a magnetic field vector (E_H). Polarization refers to the time-varying change in the orientation and magnitude of the electrical and magnetic field vectors. In most commercially available GPR systems, the transmitting antennas are dipoles designed to produce a preferred radar wave polarization (Annan, 2003; Baker et al., 2007). Antennas are normally oriented so that the electrical field vector (E_V) is parallel to the long axis (strike) of the target, to provide maximum coupling and reflection strength (Annan, 2003). The polarization direction is dependent on the antenna and dipole orientation as shown in Figure 2.4. For dipole antennas, the electrical vector E_V is parallel to the long axis of the antenna and E_H is perpendicular to the antenna length (Baker et al. 2012). When the antennas are placed in a perpendicular broadside configuration, the antenna dipole axis is perpendicular to the plane of reflection incidence and the electrical vector E_V is contained within the horizontal polarization plane (Fig. 2.4A). Another common configuration is parallel end-fire, in which the T_x-R_x pair and dipole axis are oriented parallel with the plane of incidence and E_V is contained within the vertical polarization plane (Baker et al., 2007). Vertical polarization can also be achieved by rotating broadside antennas so that their dipole axis is parallel with the direction of antenna travel (termed parallel broadside).

Conventional GPR system consist of at least one transmitting antenna (T_x) and a receiving antenna (R_x) pair (Fig. 2.3) that are either fixed at a constant separation (monostatic antenna) or positioned at variable offsets (bi-static antennas)(Fig. 2.3). The IDS Hi-BrigHT 16-channel GPR system employs two dual-polarized, arrays of ultra-wideband, ground-coupled antennas with a 2-GHz centre frequency (Fig. 2.7). The forward antenna array (elements 1-8) includes 8 antenna pairs arranged in a parallel-broadside configuration for *vertical polarization* (VV = EV mode). The second antenna array has a further 8 antennas (elements 9-16) arranged in a perpendicular broadside configuration for acquisition of *horizontally polarized* (HH = EH mode; Fig. 2.4A) data. The dual-polarized antennas are designed to allow detection of both conductive (low impedance) and high impedance dielectric targets in a single pass; linear conductive targets (e.g. metal pipes, rebar) couple strongly when they are oriented parallel with the antennas in horizontally polarized mode (HH) and low impedance dielectric targets (e.g. air-filled PVC pipes, hydrocarbons) are best imaged with vertically polarized (VV) antennas (Radzevicius et al., 2000; Simi et al., 2014). A low impedance target is one in which the target has a permittivity that is lower than the surrounding soil medium. Tree roots in dry sandy soils generally can be considered targets with a moderately large wave impedance, as the permittivity of moist roots is about 20-30 compared with 3-6 for sandy soils. This suggests that the HH (horizontal polarization) antenna array should be most effective in detecting roots.

2.2.2 Multi-channel GPR

In the last decade, multichannel GPR systems have become commercially available that employ arrays of transmitting and receiving antennas to increase the sampling density to improve target resolution and efficiency of GPR surveys (Goodman and Piro, 2013; Grasmueck and Novo, 2016). Most systems employ linear antenna arrays that allow collection of multiple lines as a single ‘swath’. These systems were developed primarily for engineering applications (investigating the structural integrity of buildings, bridge deck surveys) but the technology is now being employed in a wide range of applications (Simi et al., 2012; Goodman and Piro, 2013). In a recent study, Grasmueck and Novo (2016) evaluated full-3-D imaging using a 500 MHz multi-channel GPR system. They show that the use of GPR systems with massive, multi-channel antenna arrays can greatly increase survey efficiency and reduce the time required to conduct large surveys. However, combining GPR swaths from different surveys into a single coherent image is still a challenge. They also emphasized that reliable 3-D imaging requires that the position of each trace has to be known with high precision. Otherwise 3-D imaging will be degraded and the location of targets will be distorted (Grasmueck and Novo, 2016)

2.2.3 GPR resolution

The GPR resolution is the ability of a radar system to detect and resolve buried objects and is a function of the antenna frequency, system design, target depth and substrate characteristics (Grasmueck et al., 2005). These factors are reviewed here as they are critical to discussion of resolution capabilities of multi-channel GPR system employed in this study.

GPR resolution is often described in terms of the vertical and horizontal resolution. Vertical resolution is the smallest interval between two reflecting interfaces detectable in a radargram and is and is a function of transmitted pulse length (wavelength), signal bandwidth, and soil permittivity (Annan et al., 2003; Rial et al., 2009). The vertical resolution can be estimated using the Rayleigh quarter wavelength criteria (Fig. 2.5) (Neal, 2004):

$$\lambda_R = \frac{V}{4f}$$

where V is the radarwave velocity and f is the antenna centre frequency. In GPR studies, the vertical resolution is also commonly estimated using the effective spatial depth resolution, ΔR:

$$\Delta R \approx \frac{\tau_{pV}}{4} \quad = \quad \frac{\tau_{pC}}{4\sqrt{\varepsilon_r}}$$

where τ_p is the pulse length V the radarwave velocity, and ε_r is the relative permittivity (Annan, 2003). In practice, the vertical resolution is often used to determine the thinnest stratum for which the top and bottom of the layer can be detected. For a dry sandy soil with ε_r= 3-6, a 1-GHz antenna has a vertical resolution of about 1.2-1.7 cm (Fig. 2.5). The effective vertical resolution can be greater than the theoretical quarter wavelength limit, as the signal bandwidth contains frequencies above the antenna center frequency (Barton and Montagu, 2004).

The detection of closely-spaced roots is dependent on the horizontal resolution which is the ability of the GPR to detect closely spaced objects and is a function of the wavelength and the target depth (Annan and Cosway, 1992). The transmit beam for a typical bow-tie GPR antenna can be approximated by an elliptical beam footprint (Baker et al., 2007) with a major axis A and minor axis B:

$$A = \frac{\lambda}{4} + \frac{D}{\sqrt{\varepsilon_r - 1}}$$

$$B = \frac{A}{2}$$

where λ is the pulse wavelength, *D* is the target depth and εr the relative permittivity. As shown in Figure 2.3B, the beam footprint increases in size with target depth, and the ability to discriminate closely-spaced targets is consequently degraded. The GPR beam footprint and in turn the horizontal resolution is improved as the pulse wavelength decreases (i.e., high frequency) and as soil relative permittivity increases. Typically, a 2-GHz antenna can detect roots that are at least 1 cm apart under favorable soil conditions (Barton and Montagu, 2004; Butnor et al., 2012). Whereas a 900 MHz antenna could find roots as small as 1.9 cm in diameter if the roots in question were spaced at least 10 centimeters or more apart (Hirano et al., 2009)

The horizontal resolution of GPR system is also dependent on the inline sampling interval and inter-line spacing. GPR surveys are commonly acquired as a grid work of 2-D profiles which are interpolated to ‘quasi’ 3-D radar volumes (Grasmueck and Viggiano, 2007; Grasmueck and Novo, 2016; Molon et al., 2017). In order to achieve full-3-D GPR resolution the inline sample spacing and line density must be less than the Nyquist quarter wavelength for the transmit impulse. The Nyquist sampling interval Δx:

$$\Delta x \le \Delta x_N = \frac{\lambda}{(4 sin \alpha)}$$

where Δx_N is the Nyquist sample interval, λ is the pulse wavelength, and α is the dip angle of a plane radar wave arriving at the surface ($\alpha \approx 60^\circ$ for most antenna configurations) (Grasmueck, et al., 2005). For example, for a dry sandy soil with $\varepsilon_r = 3$ and a 1-GHz transmit frequency, the inline sample interval and line spacing must be < 2.78 cm. Most modern GPR systems are capable of sub-centimeter inline sampling but achieving inter-line profile spacing of a few centimeters is a challenge, particularly with single channel GPR system. Multi-channel GPR with multiple antenna arrays greatly simplify the collection high density surveys but even these systems are designed to collect lines with 5-10 cm line separation. Collection of line at 2 cm separation requires careful survey layout, precise survey navigation and the use of overlapping multi-channel coverage to allow high density GPR swathing. If the GPR survey design does not meet the Nyquist sampling intervals, the interpolated 3-D volume can suffer from distortions due to spatial aliasing of high frequencies and steeply dipping reflectors (Grasmueck et al., 2005). The trace sampling rate (vertical trace sampling) must also satisfy the Nyquist criterion in order to avoid signal aliasing but most modern GPR systems employ digital oversampling or Nyquist filters to ensure that the signal is not aliased.

2.3 IDS Hi-BrigHT Multichannel GPR

GPR data were acquired using the IDS Hi-BrigHT multichannel GPR system (Fig. 2.6). The Hi-BrigHT is a 16-channel 2-GHz system developed originally for high-resolution bridge deck survey and rebar detection. The antenna module integrates two arrays of ultra-wide band, high-frequency ground-coupled antennas (Fig. 2.7). The Hi-BrigHT antenna array consists of two parallel arrays of horizontally (HH) and vertically polarized (VV) antenna pairs (8 in each array) separated at 10 cm intervals (Fig. 2.7). The antenna has a 91 x 42 cm footprint, a surface area of about 0.3 m^2 and weighs approximately 35 kg.

The Hi-BrigHT can collect 16 profiles (8 HH, 8 VV) within a single swath. The profiles have a 10-cm separation, resulting in a total a swath width of 70 cm. The dual polarizations of the antenna arrays allow for the detection of different kinds of targets using a single GPR system.

The Hi-BrigHT is housed on a trolley which carries the antennas in a shielded case with an abrasion resistant base (Fig. 2.6). The antenna module is controlled by two signal generation and digital-to-analog converters (DAD, or the radar control group) which provide scan rate of up to 512 samples scan. The trolley also houses dual batteries and a laptop display for data acquisition. This allows the user to receive real-time data recordings and to make any adjustments necessary during the survey (Simi et al., 2012)

2.4 Multi-channel GPR surveys

High-resolution multi-channel GPR surveys were conducted at both test sites using the Hi-BrigHT 2-GHz GPR with a conventional grid survey pattern (Fig. 2.9). GPR swaths were collected by manually pushing the GPR cart across the survey area while maintaining the right edge of the antenna array in contact with the guide rail system. Lines were acquired with a 2-cm cross-line spacing and an inline sample interval of 0.4 cm (250 scans per metre). 2-cm was the minimum line spacing that could be achieved using guide rail system and overlapping swaths. This line interval approximates the Nyquist quarter-wavelength sampling interval for a 2-GHz antenna (1.7 cm for a dry sandy soil; Fig. 2.5) required for full-3-D GPR resolution (Grasmueck et al., 2005). The survey was performed in both the X- and Y-directions providing complete coverage of the 25-m^2 survey patch except for a 1 m^2 area in the center containing the tree trunk, which could not be surveyed (Fig. 2.9). Both HH and VV profiles were acquired simultaneously.

The swathing pattern used to obtain 2 cm overlapping coverage is shown in Fig. 2.8. A total of five swaths (8 VV and HH inline profiles) were acquired at a 2-cm separation and the GPR system and guide rail were moved 90 cm to the left to the beginning of the next swath set.

The radar profiles were recorded with a 17.57 ns record length and 512 samples per trace in proprietary IDS format and naming convention. The IDS files have an 8-digit name starting with the line direction, longitudinal (LI) or transversal (Tl). Following the direction prefix is a two-digit antenna number (01 to 16) and the last four digits indicate the line number. An example of a line name is as follows: Tl070042. This indicates a transversal line direction, collected by antenna seven, and forty second line in the survey.

2.5 GPR processing

Multichannel GPR data were processed using GPR-SLICE v7.1 using a customized processing flow (Fig. 2.10). GPR-SLICE software includes modules for basic radargram editing and filtering and interpolation of profiles to 3-D radar amplitude volumes (Goodman and Piro, 2006). The processing steps are described in the following sections and the processing results are discussed in section 3.1. A summary of radargram processing is provided by Jol et al. (2003).

2.5.1 Radargram import, editing, background removal

Radargrams were imported to GPR-SLICE in the IDS proprietary format (*.dt1) and a zero-time correction was applied to account for drift in the direct wave arrival time. A dewow filter was applied during import to remove low frequency (DC) signal bias. These low frequency components are often produced inductive coupling of the antennas or by saturation of the signal amplifiers by large amplitude airwave/ground wave arrivals (Annan, 1993; Cassidy, 2009). The dewow operation in GPR-SLICE employs high-pass filter which produces a zero-mean trace. Following radargram import, a zero-time correction was applied to account for drift in the direct (air) wave arrival time. Zero time errors result from drift due to changes in instrument temperature, cable length differences, and the varying antenna ground surface air gap. Zero-time errors due to incomplete coupling of the antenna to the ground surface are a particular problem when using antennas with a large surface area on uneven ground. The software employs a sliding search window to detect the onset of the direct wave pulse, and each radar trace is shifted to the 0-nanosecond position in the record.

A background subtraction filter was then applied to suppress horizontal banding resulting from direct wave ringing that is common in radargrams (Fisher et al., 1992; Annan et al., 2003; Kim et al., 2007). The filter operator calculates the average trace across entire radargram and subtracts it from each trace. Direct and groundwave arrivals add constructively in the average trace and they are cancelled by mean trace subtraction. This step effectively removes horizontal banding due to ringing but can also degrade horizontal reflections from permittivity boundaries(i.e., due to sediment layering)(Goodman, 2016). In this study, the removal of horizontal reflections produced by soil layering was found to be beneficial to resolving root targets

2.5.2 Gain, bandpass, boxcar filtering

Signal gain filter was applied to all radargrams to recover amplitude losses due to spherical divergence and attenuation losses (Annan, 2003; Goodman and Piro, 2013). The filter employed a simple linear function to boost the signal in the upper 5 ns of the record. A bandpass filter (1500-3000 MHz) was then applied reduce low-frequency reverberation and noise produced by antenna lift-off. As a final step, a boxcar averaging filter (3 fiducials) was applied to smooth radargrams and further reduce high frequency noise (Goodman, 2016).

2.5.3 Velocity analysis

The radarwave velocity was determined for several radargrams in each dataset by fitting a hyperbolic function to several root diffractions at various depths. Velocity data are required for radargram depth conversion and for subsequent migration operations. The velocity fitting algorithm employed in GPR-SLICE is an equation of the form:

$$V = \frac{2\left(\sqrt{x^2 + (d + r)^2} - r\right)}{t}$$

where *V* is root-mean square (average) velocity, *x* is the offset distance from the transmitter to diffraction apex, *r* is the root diameter, *d* is the depth to the target (root) top surface and *t* is the two-way travel time (Annan, 2003). The velocity is determined in GPR-SLICE by fitting a hyperbolic curve ('rubber band') to the diffraction at several locations (Fig. 3.3).

2.5.4 Migration

Migration is a process applied to seismic and GPR data, which repositions reflections and diffractions to their true subsurface locations (Fisher et al., 1992; Reynolds, 2002). As shown in Fig. 1.2, root diffractions appear on a radargram as hyperbolic arrivals, because the two-way travel time of the radarwave varies with the offset distance (x) between the buried object and the GPR antenna. The two-way travel time is at a minimum when the antenna is directly over the object (x=0) and increases with increasing offset distance. Migration moves dipping reflections to their true subsurface locations and collapses diffraction events to a single point source. This is a critical step in root detection, as it allows the subsurface location of the root diffraction point to be determined (Fisher et al., 1992).

Radagrams were migrated using an implementation of 2-D Kirchoff migration in GPR-SLICE (Fisher et al., 1992; Moran et al., 2000). Kirchoff migration employs an integral solution of the wave equation to reconstruct the downgoing (transmit) and upgoing wavefield. The migration velocities were set using the velocity profile determined by curve-fitting.

2.5.5 Hilbert transform

As a final processing step, a 2-D Hilbert transform was applied to all migrated radargrams to enhance imaging of root diffractions. The Hilbert operator implemented in GPR-SLICE calculates the instantaneous amplitude of the radar trace envelope (Liu and Oristaglio, 1998; Luo et al., 2003) as:

$$a(t) = \sqrt{[s(t)^2 + s^*(t)^2]}$$

where s(t) is the trace time series and s*(t) is the imaginary trace component:

$$s(t) = a(t)cosv(t)$$

$$s^*(t) = a(t)sinv(t)$$

The instantaneous amplitude (Hilbert trace) is rectified (positive in value) and when calculated on migrated radargrams it produces discrete amplitude foci, which are centered over the collapsed point of each diffraction apex (Fig. 1.2D). For cylindrical objects, such as roots, the Hilbert amplitude focus produces a pseudo-cross-sectional area of the object (Fig. 1.2D), which is more amenable to interpolation to a 3-D volume and visualization as isometric surface using marching cubes or by simple thresholding of the amplitude values (Goodman, 2016).

2.5.6 Radargram interpolation and 3-D volume generation

2-D radargrams were interpolated to 3-D radar volumes using two different algorithms in GPR-SLICE, inverse-distance weighted (IDW) gridding and kriging. The IDW method estimates the grid nodes around known data values using weighted points within a pre-set search radius (Shepard, 1968). The IDW algorithm implement in GPR-SLICE is the modified Sheppard method, in which the estimated value u(x) is calculated as:

$$u(x) = \frac{\sum_{i=0}^{n} \quad \frac{u_i}{d(x, x_i)^p}}{\sum_{i=0}^{n} \quad \frac{1}{d(x, x_i)^p}}$$

where u_i is the ith data point of n data samples, $d(x, xi)$ is the Euclidean distance between the estimated value and each data point and the exponent p is the inverse distance weighting factor. Small values of p (< 2) give a greater weighting to more distant data points, resulting in smoothing of the interpolated surface (Goodman, 2016).

Kriging is a geostatistical interpolation method that takes into consideration the spatial correlation of variables under estimation. Like IDW methods, Kriging employs a weighted average of neighboring values to estimate an unknown grid value but the weightings are optimized using a semi-variogram model to quantify the variance between data points. This is done by using a Gaussian process with predetermined covariance, or variables, to estimate a linear prediction that may not always value external criteria, such as smoothness (Goodman, 2016). GPR Slice uses a modified equation describing Kriging as follows;

$$Data\ Weights = c^{-1}d$$

Where the value for c will vary based on the distance between points in question, nugget value (a smoothing factor), and the range of the covariance values and d represents the vector between the points in the estimate to be interpolated (Goodman, 2016).

In order to optimize the gridding parameters both interpolation methods were tested on a small 2 x 2 m subset of the R4HH data set (Fig. 2.2). The grid cell size (0.5-2 cm), search radius and smoothing factors (inverse distance weighting factor; kriging nugget) were varied to determine which parameter values produced the most coherent images and continuous root networks.

Search radius values of 0.01, 0.02, 0.05 and 0.1 m were tested for various grid cell sizes (0.5-2 cm) and 3-D radar volumes were interpolated.

2.5.7 Root isosurface modelling

Isosurface models of root networks were generated from the Hilbert 3-D radar volumes using the Marching Cubes Algorithm (MCA) (Lorensen and Cline, 1987; Neuman and Yi, 2006; Molon et al., 2017). MCA is an algorithm used to extract isosurfaces or surfaces of equal value (amplitude) from a 3-D lattice of scalar values. The vertices of voxel elements (8 for a cube) in the 3-D grid mesh are assigned a value relative to a user defined threshold. Any vertex of the cube that is less than or equal to the minimum defined amplitude is said to be outside the surface. Any values that are greater than the defined threshold is said to be inside the surface. Voxel elements that are inside the surface are then summed and their total volume is calculated (Molon et al., 2017). Isosurface volumes were created in Voxler 4 software. In this study, quantitative estimation of root biomass was beyond the scope of the work, and the threshold amplitude for the isosurfaces were chosen arbitrarily based upon visual inspection of the root network. Quantitative estimation of biomass (i.e., root volume) can be obtained from the isosurfaces, but the threshold amplitude must be calibrated against roots of known diameter (e.g. Molon et al., 2017).

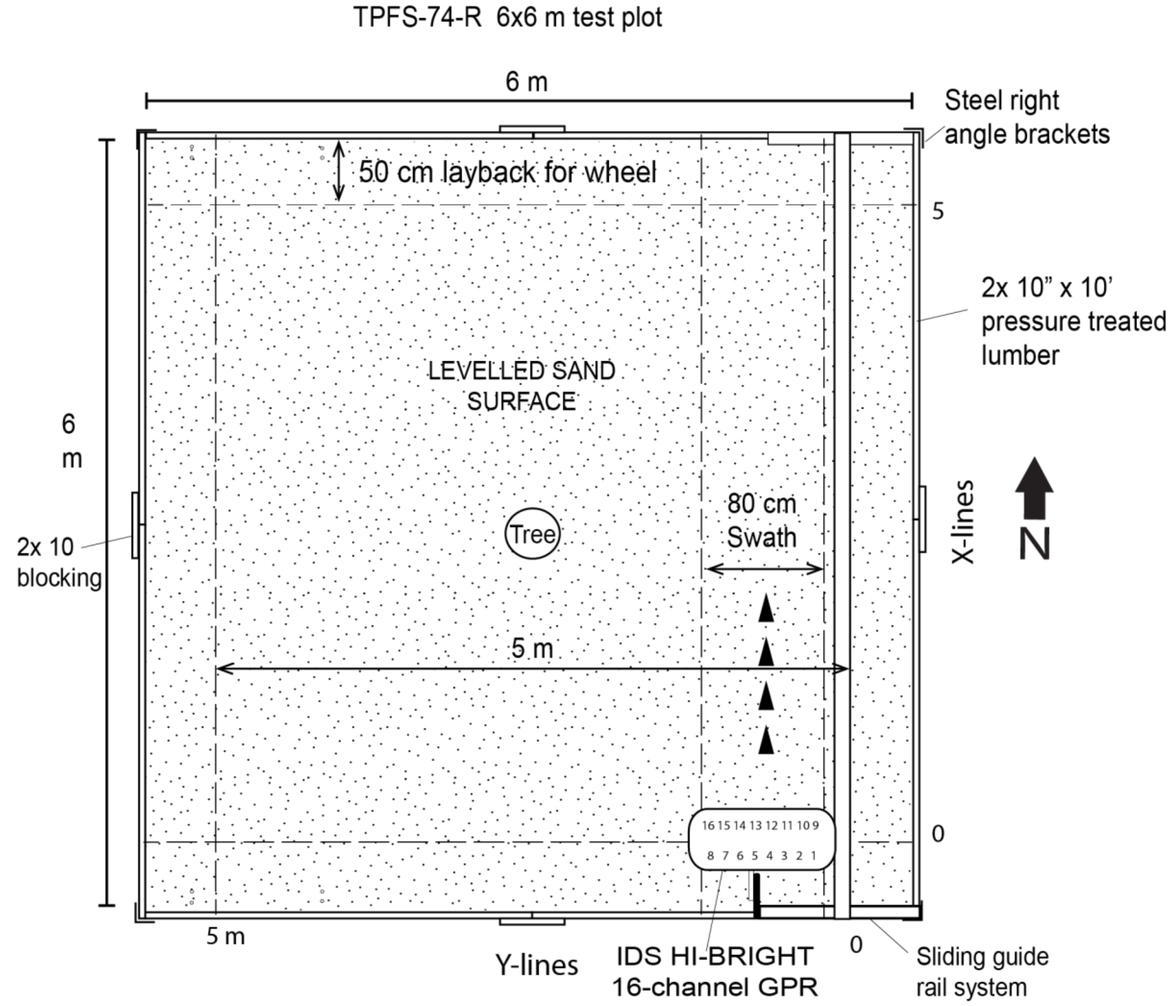

Figure 2.1: Schematic showing the layout of the TPFS-74-R (Romeo) test site. The GPR system was navigated in X, Y directions using guide rail system and inline positions recorded with an odometer wheel.

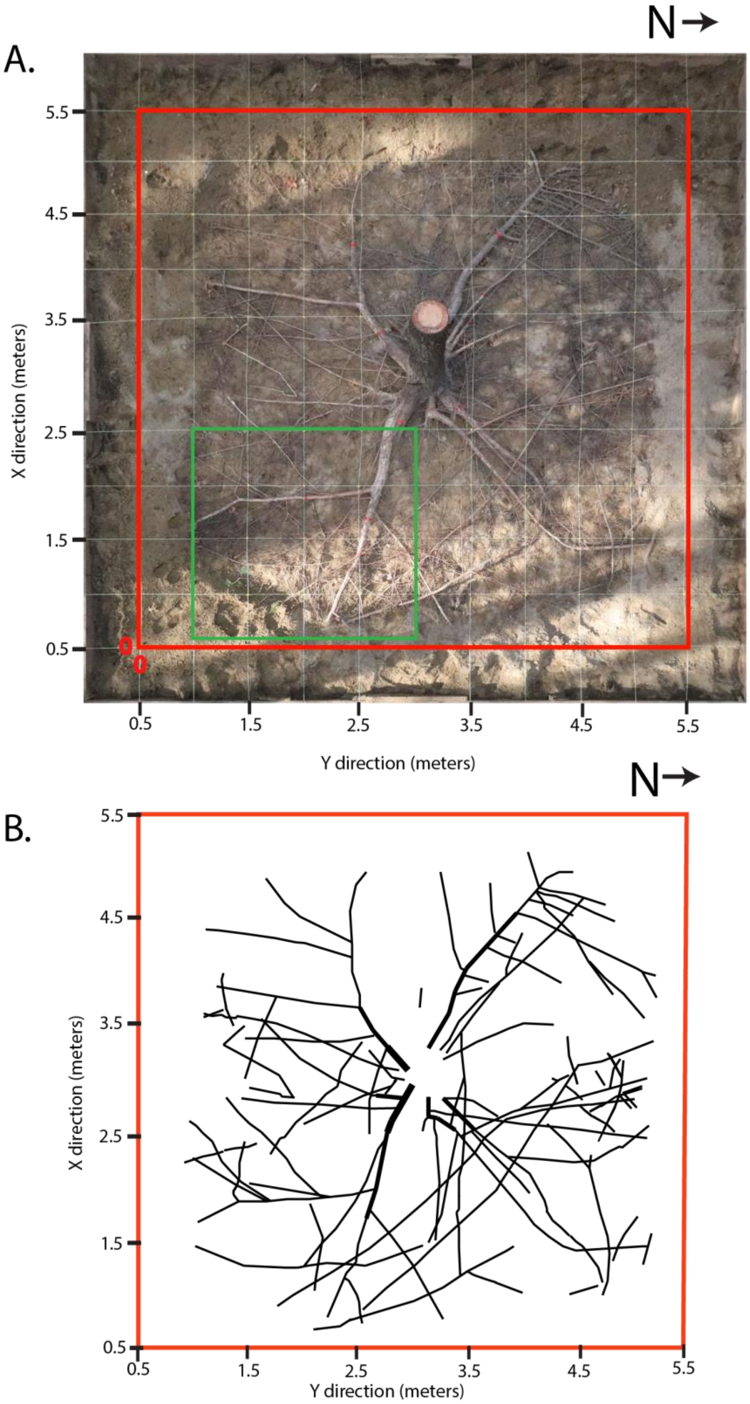

Figure 2.2. (A) Orthorectified photo of TP74-R, showing exposed root network. 25-m^2 GPR survey patch outlined in red. Reference grid spacing 0.5 m. Subset area (X: 1-3 m; Y: 0.61-2.5 m) used to test gridding parameters shown in lower right part of survey grid. (B) Vectorized root network for 25-m^2 area shown above.

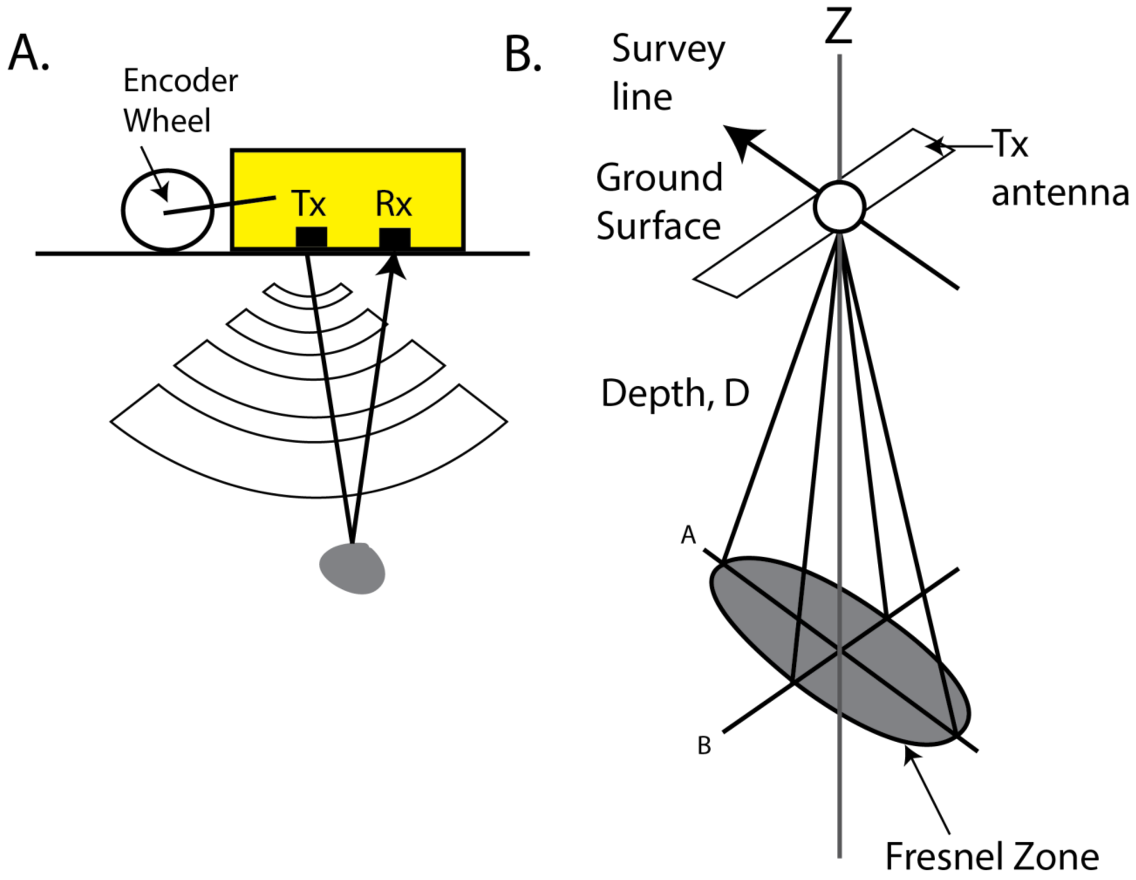

Figure 2.3: (A) Monostatic GPR antenna. (B) Transmit beam footprint can be approximated by an ellipse with major axis A and semi-major axis B.

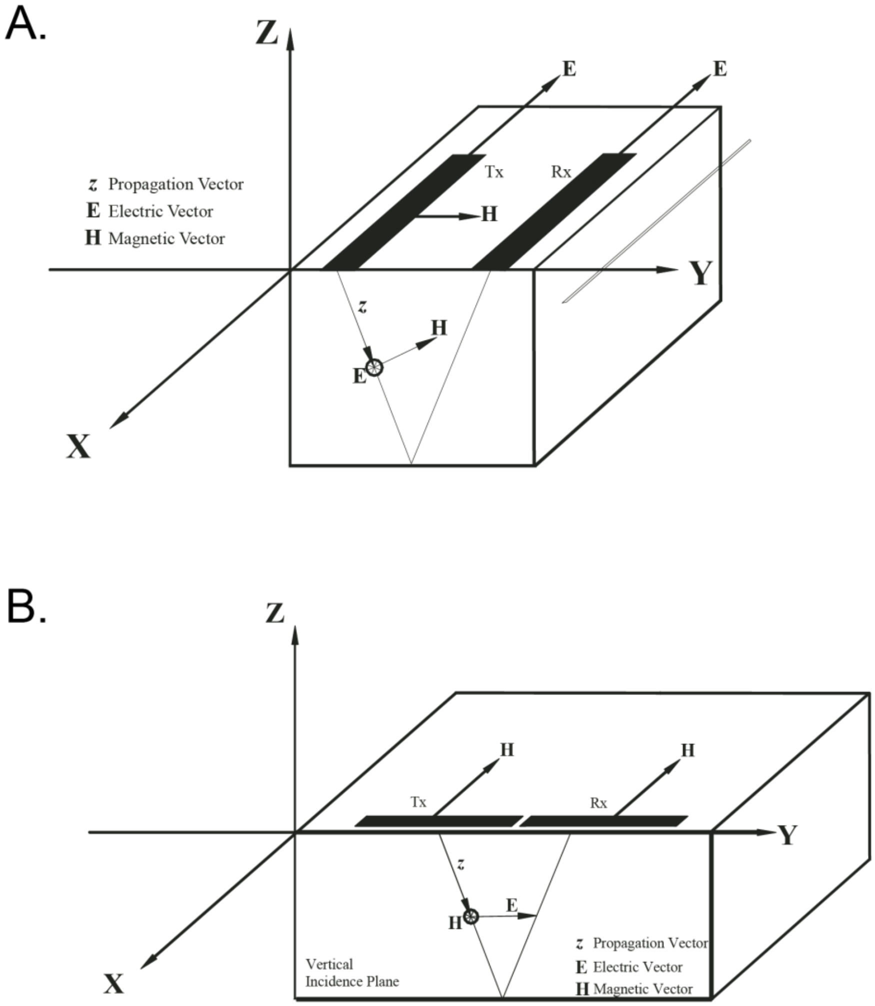

Figure 2.4: (A) Broadside antenna configuration. Electrical vector (E) contained within horizontal polarization plane (EH or HH mode). (B) End-fire antenna orientation, with antennas parallel to profile and electrical vector (E) in the vertical polarization plane (EV or VV mode). From Baker and Jol (2007).

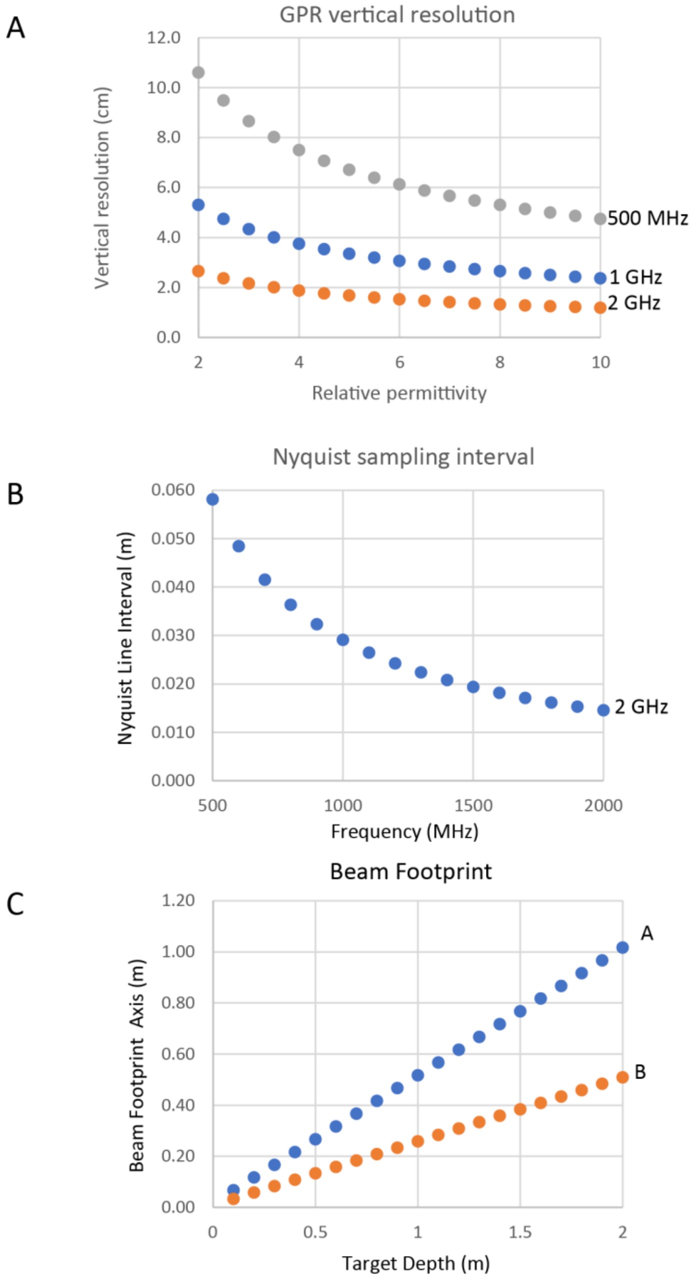

Figure 2.5: (A) Vertical resolution as a function of antenna centre frequency. (B) Nyquist line interval for centre frequency of 2-GHz. Note the Nyquist sampling interval is approximately 1.75 cm. (C) Variation in GPR beam foot print with

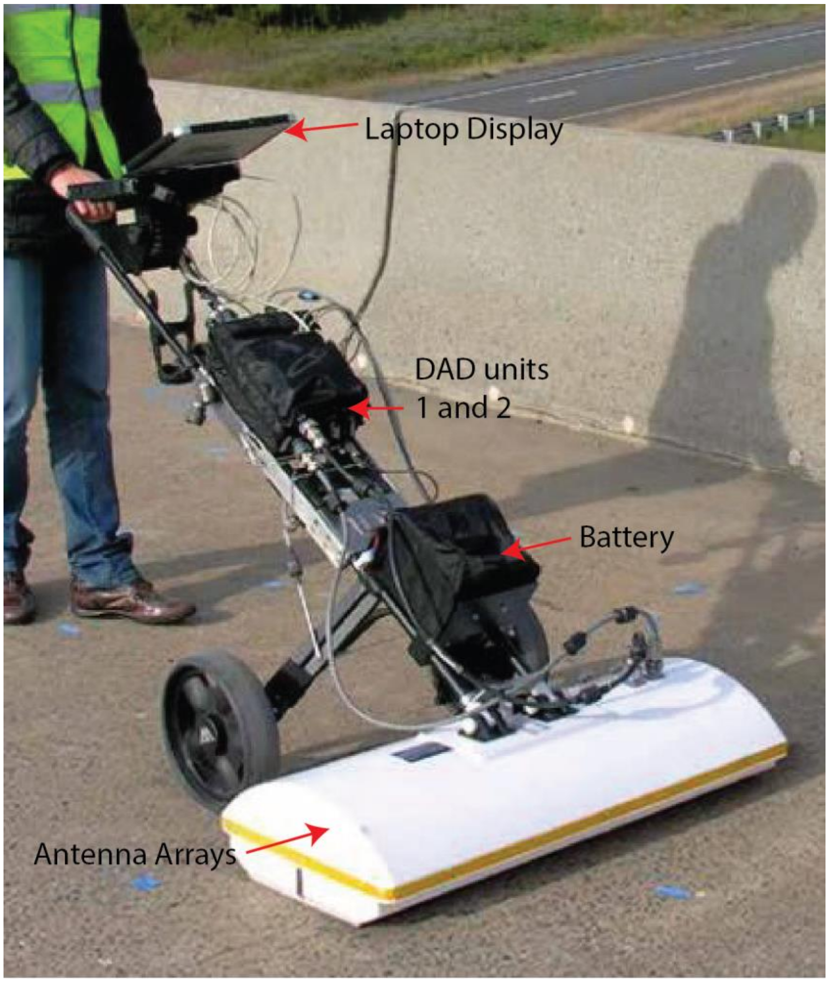

Figure 2.6: Hi-BrigHT multichannel GPR system. The system includes a 16-channel dual-polarized antenna array mounted on a two-wheel trolley. Inline sampling position is recorded by an odometer wheel.

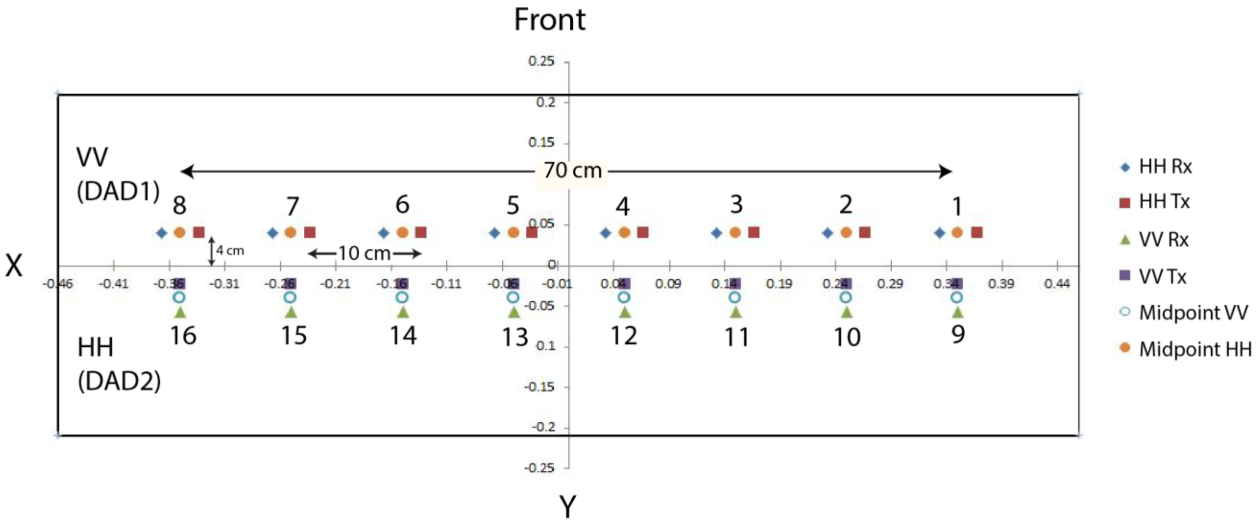

Figure 2.7: Schematic showing internal configuration of dual polarized antenna arrays in Hi-Bright system. HH= horizontal polarization. VV = vertical polarization. Note antenna elements are numbered from right to left.

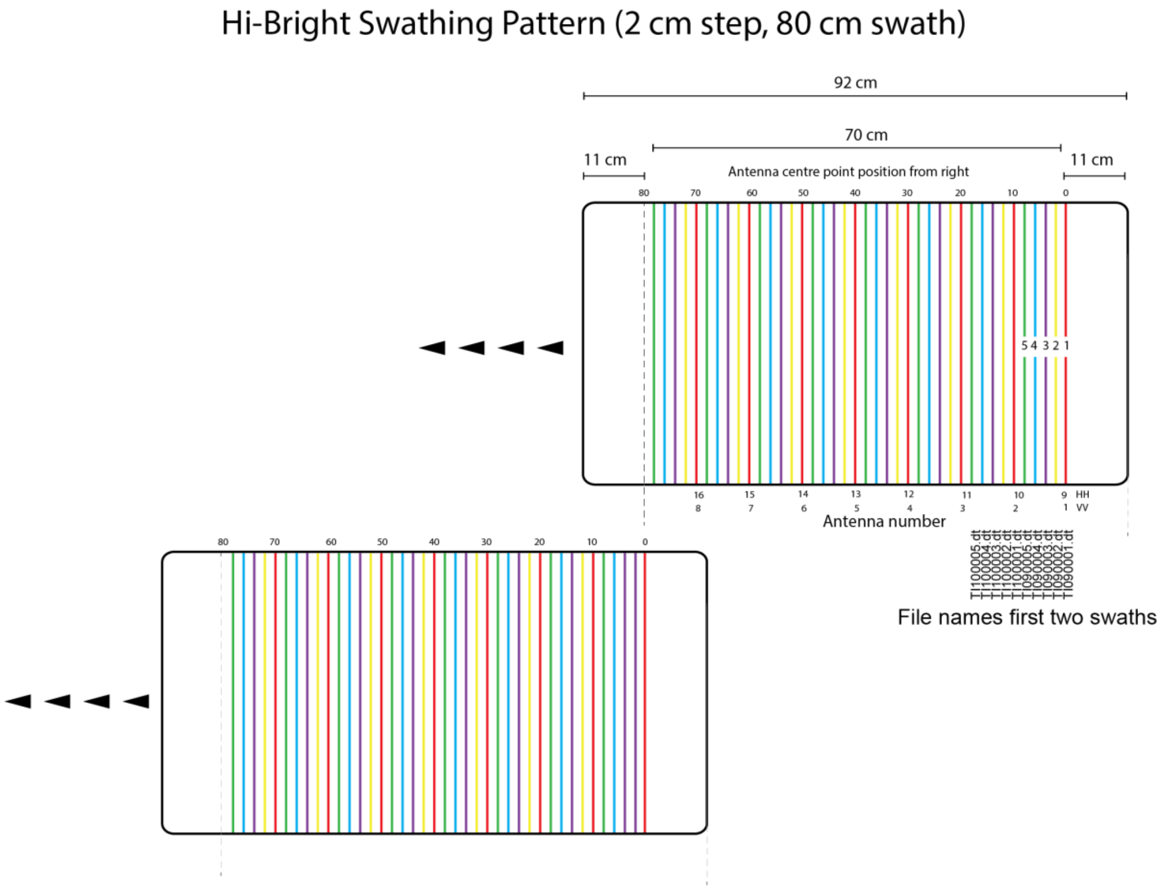

Figure 2.8: Schematic showing the swathing pattern employed at both test sites to acquire overlapping swaths (2-cm line spacing) with the Hi-BrigHT antenna.

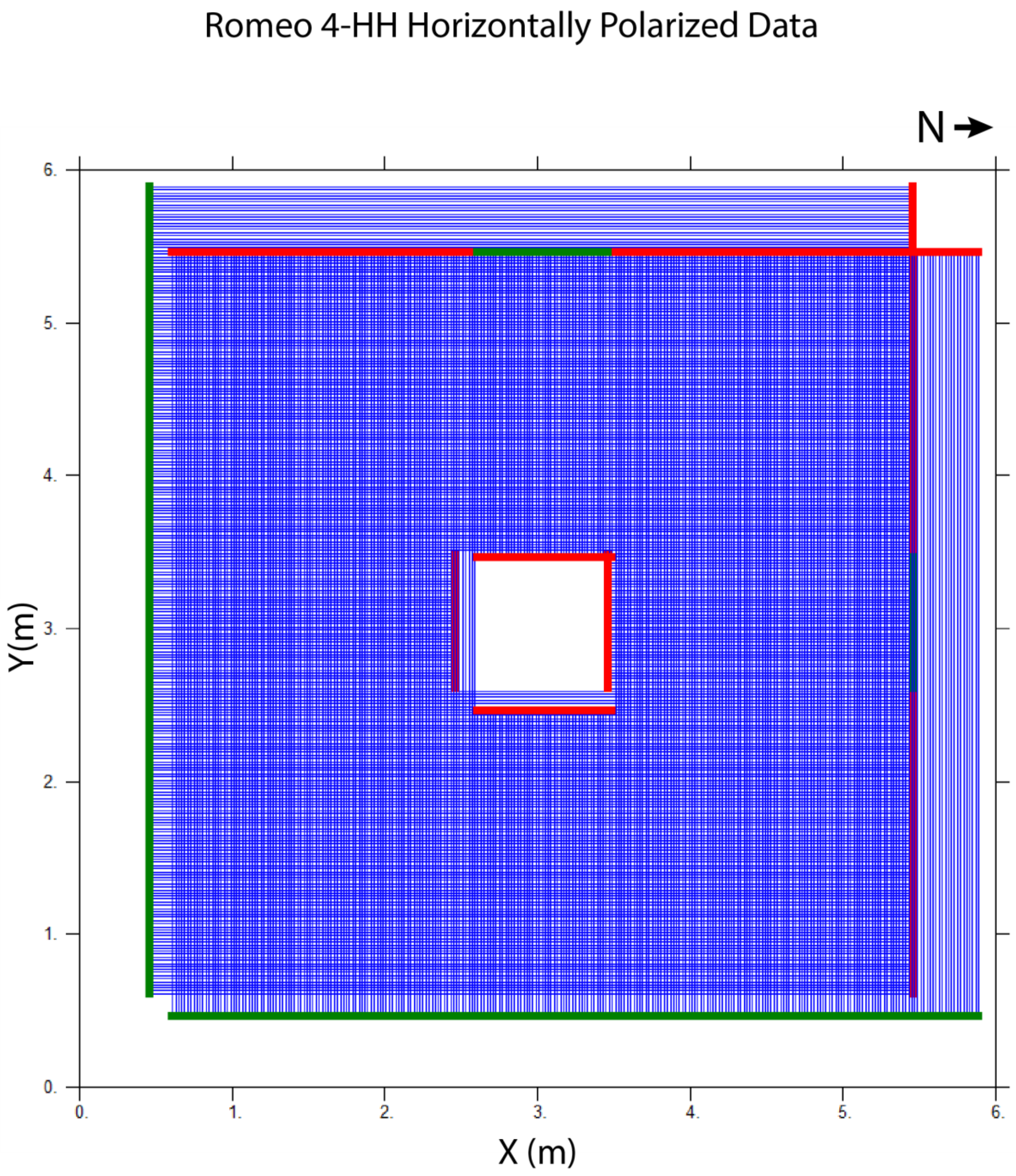

Figure 2.9: Survey grid showing survey line paths at site TPFS-74-R. Line spacing is 2 cm.

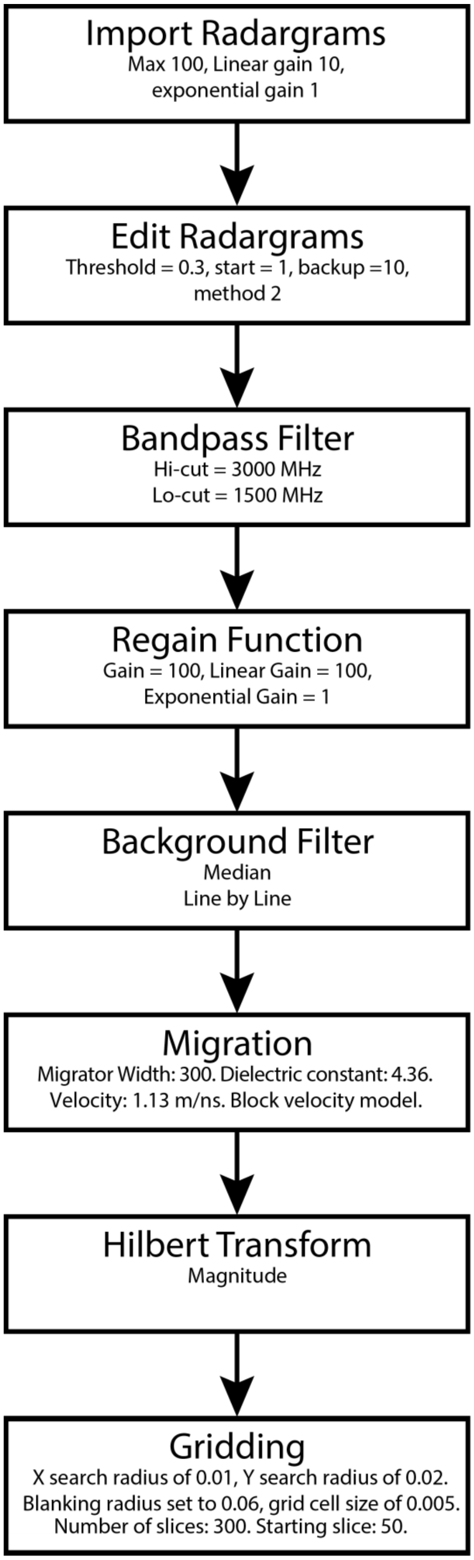

Import Radargrams
Max 100, Linear gain 10, exponential gain 1

Edit Radargrams
Threshold = 0.3, start = 1, backup =10, method 2

Bandpass Filter
Hi-cut = 3000 MHz
Lo-cut = 1500 MHz

Regain Function
Gain = 100, Linear Gain = 100, Exponential Gain = 1

Background Filter
Median
Line by Line

Migration
Migrator Width: 300. Dielectric constant: 4.36. Velocity: 1.13 m/ns. Block velocity model.

Hilbert Transform
Magnitude

Gridding
X search radius of 0.01, Y search radius of 0.02. Blanking radius set to 0.06, grid cell size of 0.005. Number of slices: 300. Starting slice: 50.

Figure 2.10: Schematic showing GPR processing steps in GPR-SLICE software.

Chapter 3: Results

3.1 Radargram Processing

3.1.1 Filtered radargrams

Figure 3.1 shows the results of radargram zero-time corrections and dewow filtering. The airwave/groundwave arrival is represented by the high amplitude arrival at 1-1.2 ns. Several vertically-oriented 'stripes' of high (negative) amplitude noise are present on the radargram, which result from incomplete coupling of the radar antenna with the ground surface. It was observed during field data collection that the noise artifacts were produced by the uneven surface of the survey area, which caused the antenna to temporary lift off and decouple from the ground surface. The application of a band-pass (1.5-3 GHz; Fig. 3.2) was effective in suppressing the antenna decoupling noise but some coherency loss was present in the first 2-3 ns of the radargrams where the noise was present. Background filtering was effective in removing horizontal ringing in radargrams, particularly in the interval 2-6 ns, which was heavily banded with airwave ringing (Fig. 3.2B).

3.1.2 Velocity analysis

The velocity analysis was performed by fitting of hyperbolic curves to diffraction events on the filtered radargrams (Fig. 3.3). Through testing of several velocity values, it was determined that a simple two-layer model provided the best fit. The upper layer velocity was 0.7 m/ns and increased to 1.13-1.15 m/ns at a depth of around 4-5 cm centimeters in the record. This velocity increase can be accounted for by a change in soil relative permittivity associated with changing composition and/or moisture content. The upper low velocity layer likely represents a more moist organic-rich (i.e., leaf litter), high permittivity layer, and overlying well-sorted sand with lower moisture content (Figure 3.3). The two-layer velocity model was employed to depth-correct all radargrams and 3-D radar volumes.

3.1.3 Migration and Hilbert-transformation

Figure 3.5A shows the results of Kirchoff migration. The migration function successfully collapsed most root diffractions, producing a local amplitude foci at the true subsurface location of buried root (Fig. 3.4). However, some root diffractions showed incomplete migration and were not collapsed completely, particularly where diffraction events were clustered (i.e., closely-spaced roots) or at shallow depth. Incomplete diffraction collapse also results from roots that are oriented obliquely to the survey line, as the root angle affects both the diffraction amplitude and hyperbolic curvature (Tanikawa et al., 2015). Migration may also fail due to lateral or vertical variations in soil velocity. In areas of vertically stacked roots, the overlap between diffractions results in a complex radargram, which does not collapse completely with migration.

Figure 3.5B shows the Hilbert-transformed radargram. The transform produces amplitude foci centered over the migrated diffractions, which greatly simplifies imaging and interpretation of roots in the radargram. The envelope calculation also enhances the discrimination of closely-spaced roots (for example at X= 2 m; Fig. 3.15B) that are not imaged in the migrated radargram. The Hilbert radargrams were employed in subsequent step to produce 3-D radar volumes and to model the root network using isosurfaces. The Hilbert amplitude foci, when calibrated against roots of known diameter can also be used to estimate root biomass (Molon et al., 2017).

3.2. Gridding and Interpolation

Prior to gridding the entire dataset, several test 3-D volumes were created using a 4-m^2 subset of the R4HH and R4VV datasets (Figure 2.2). In order to evaluate the gridding algorithms, a 4-m^2 subset of the R4HH dataset was interpolated using both inverse distance weighted (IDW) and a Kriging algorithms with identical grid parameters (X-search radius = 0.1, a Y-search radius= 0.02, and a blanking radius = 0.06) (Fig. 3.6). The two interpolation methods yielded nearly identical results (Fig. 3.6) but the processing time with Kriging was substantially longer, taking up to 8 hours to grid a 5 x 5 m radar volume, compared with fifteen to thirty-minute interpolation time using IDW. Consequently, IDW interpolation was used for all subsequent gridding of 3-D GPR volumes.

In a second step, the search radius was tested for values of r = 0.01, 0.02, 0.05 and 0.1. A search radius of 0.05 (Fig. 3.7C) provided the best image coherency, removing high-frequency noise and improving the overall continuity of root segments. The search radius of 0.1 m over-smoothed the data and reduced the amplitude of some of the smaller diameter roots (Fig. 3.7D). Too small a search radius resulted in a lack of continuity of roots and produced high-frequency noise in the grids.

Figure 3.8 shows a comparison of the depth slices for the interpolated X-line and Y-line data for the R4HH 4-m^2 area. The time slices show two distinct sets of roots with different orientations. The X-line data imaged roots with angles of about 70-90° to the x-axis (Fig. 3.8A). The Y-lines imaged roots with preferred angles of about 0-30° of the x-axis. It is also noted that roots that are perpendicular to the X-lines are not imaged in the Y-direction data and vice versa. These data clearly demonstrate how the root orientation affects root detection and root network mapping. The depth slices in Figure 3.8 also demonstrate the effects of navigation errors on the image quality. Several root segments show offset ‘zig-zag’ noise produced by slippage of the survey wheel. These offsets are systematic errors cannot be compensated by filtering.

Figure 3.9 compares depth slices for the horizontally polarized (HH) versus vertically polarized (VV) antennas. It is clear that the HH polarized data provides a sharper and more coherent image; a larger number of roots are detected compared to the VV polarization. Root orientation also plays a significant role as discussed earlier.

As a final evaluation step, the orientation of roots within the 4-m^2 subset were compared with the root network (Fig. 2.2). Depth slices are shown in Figure 3.10 at 11 cm, 13 cm, and 16 cm depth for comparison with the vectorized root network (Fig. 3.11D). A number of large coarse roots are correctly imaged but many small diameter roots are below the resolution or are imaged incompletely due to root orientation.

3.3 3-D GPR Volumes

3-D GPR radar volumes were compiled for the horizontal (R4HH) and vertically polarized (R4VV) data for the 5 x 5 m TP74-R survey site using IDW interpolation. The X-line and Y-line datasets were first gridded separately to produce X and Y GPR volumes and then gridded together using the combined XY datasets for both antenna polarizations. The completed 3-D volumes for the R4HH X- and Y-lines are shown in Figure 3.11. The images reveal a radial root network with a large number of continuous coarse root segments. The rooting zone is located between 5-40 cm depth, with the highest root density occurring at 10-20 cm depth. Like the test area results (Fig. 3.9), the completed 5 x 5 m volumes show that root orientation strongly controls root detection; root orientations in the R4HH-X dataset are oriented predominantly perpendicular to the x-axis and detected roots in the R4HH-Y are mainly parallel to the x-axis.

3.3.1 R4HH-XY GPR volume

Figure 3.12 shows selected depth slices produced by interpolation of the combined X- and Y-lines for the R4HH-XY dataset (Figure. 3.12). Time slices were taken at equal 5 cm intervals for the depth range 5 to 20 centimetres. The time slices image the majority of the coarse white pine roots; comparison with the root network photo suggest that roots >3-5 cm can be mapped as continuous root structures. The highest frequency of roots was found at about 10 cm depth. Large roots >3 cm were detected while small roots < 1 cm evaded detection at this resolution. In some areas of the grid it was noted that the interpolation of the combined X- and Y-lines resulted in the loss of root detection (Fig. 3.12). The loss of image coherency is attributed to positioning errors produced by survey wheel slippage. The wheel slippage resulted in the mislocation of traces in the X- and Y-line datasets, which when gridded produced destructive interference of amplitudes in the GPR depth slices.

3.3.2 R4VV-XY GPR Volume

Figure 3.13 shows the combined R4VV-XY depth slices for the same depth intervals (5-20 cm). The R4VV time display a large portion of the coarse root network, with the highest root frequency between 10 and 15 cm depth. However, there are many more large roots present at a depth of 15 centimeters in this volume than in the R4HH volume. Though there are more roots at this depth in the lower left quadrant they appear much larger diameter than those seen at the previous depth. This could indicate constructive interference/addition of amplitudes from multiple closely-spaced roots giving the illusion of large roots. This is the most likely scenario as the excavation did not find any large roots in this location. Overall, the R4VV volume successfully images roots, but at a lower clarity than that of the R4HH volume.

3.4 3-D Isosurface Models

The combined X- and Y-line GPR volumes (Figs. 3.12, 3.13) show that a large proportion of very coarse roots can be detected and mapped but many areas of the combined grid show the effects of destructive interference. One possible solution to this problem is to generate isosurface models for the X- and Y-lines separately and combine them. Isosurface models for the HH and VV datasets are shown in Figures 3.14 and 3.15. The isosurfaces were generated by gridding of X-line and Y-line data separately using the IDW algorithm in Voxler software. The X-line interpolation is shown in green and the Y-line data in orange. The isosurface threshold (amplitude cut-off) was set arbitrarily at a value which matched the approximate root diameter and produced the best root continuity.

The horizontally polarized data (R4HH; Fig. 3.14) produced the most-coherent-looking root isosurface model (Figure. 3.14). Many continuous roots were imaged but many small point targets were also detected; these may represent small or partially detected root segments or diffractions produced by other targets in the soil column (e.g. organic debris, dead roots). The horizontally polarized data detected a majority of roots >= 2 cm in diameter, as long as the root orientation was within detection angle limit (Fig. 3.12). Roots that were smaller than 2 cm in diameter were not imaged well in the isosurface. In some cases, the X and Y datasets were able to partially detect a root that was not oriented well in a single datasets and thus could not fully pinpoint its size and location. When the two datasets were combined these partially-detected roots were much easier to distinguish.

The vertically polarized data (R4VV) generated a much less coherent isosurface and 3-D volume (Fig 3.15). While Figure 3.14 (HH dataset) shows a number of continuous root structures, the vertically polarized data failed to image even the largest of roots in the study site (Fig. 3.13, Fig. 3.15). The vertically polarized data struggled to attain the same level of detail and clarity that the horizontally polarized data produced and was limited to detecting the larger main roots of the network (Fig. 3.13B, C).

The horizontally polarized data imaged roots clearly in both the X and Y directions while the vertically polarized data only imaged the Y direction clearly (the X direction had roots imaged but not to the same level of clarity).

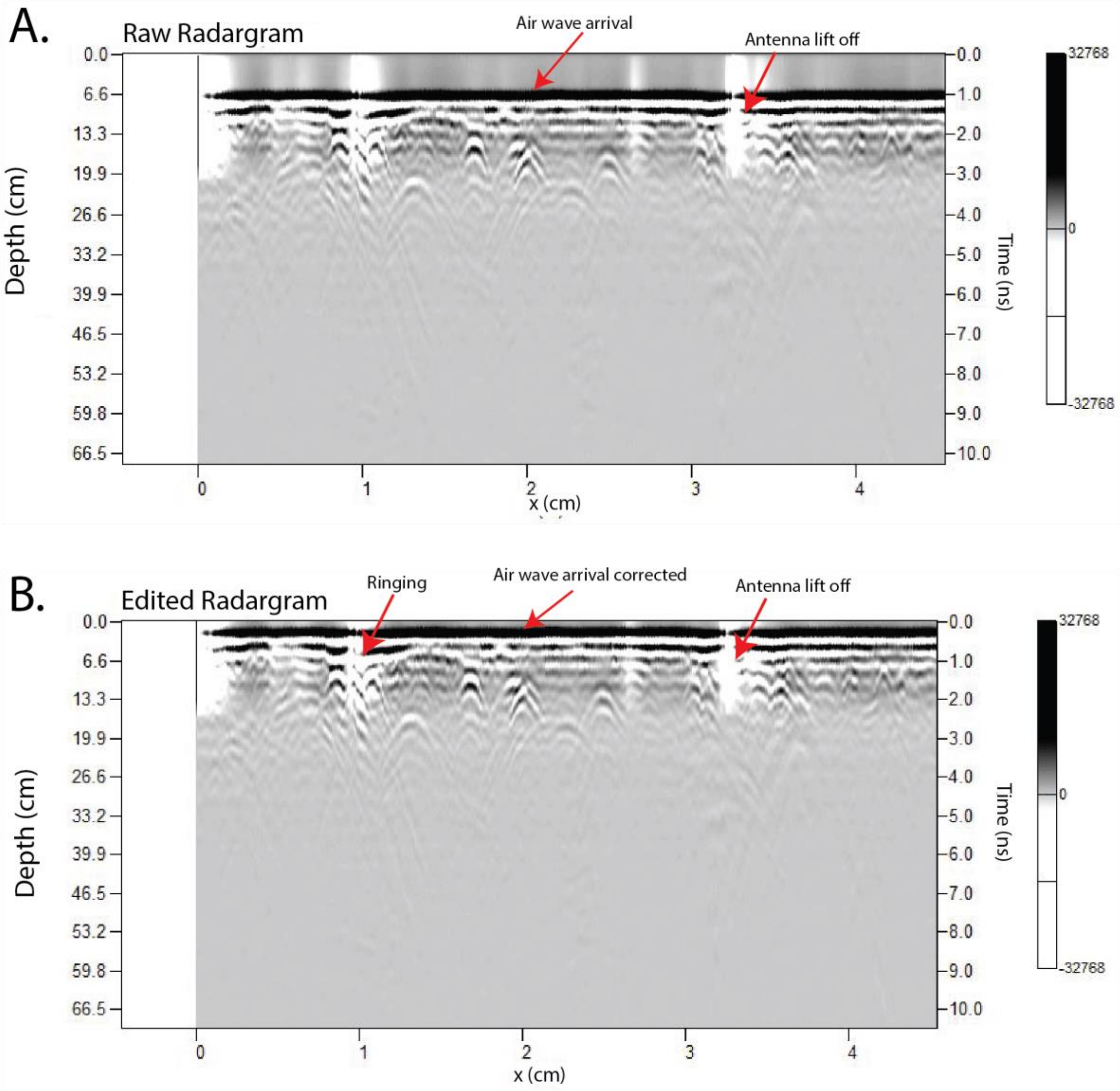

Figure 3.1: (A) Unprocessed radargram. Note long wavelength, high-amplitude noise in first 1-2 ns of record due to antenna lift off and saturation of amplifier. (B) Edited radargam with dewow filter applied.

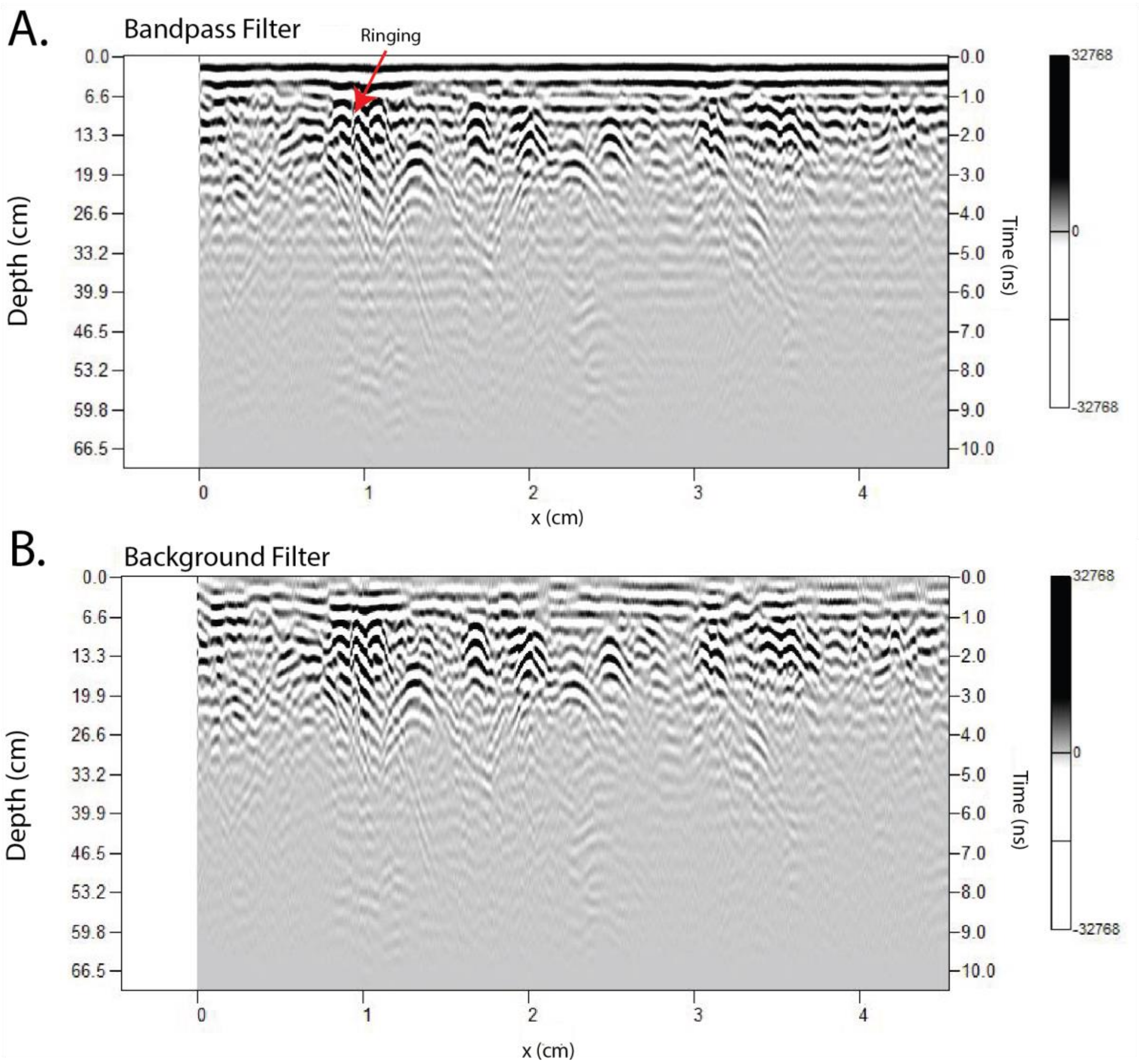

Figure 3.2 (A) Bandpass filtered radargram (1500-3000 MHz) (B) Background removal filter applied to suppress ringing and airwave/ground-coupled wave.

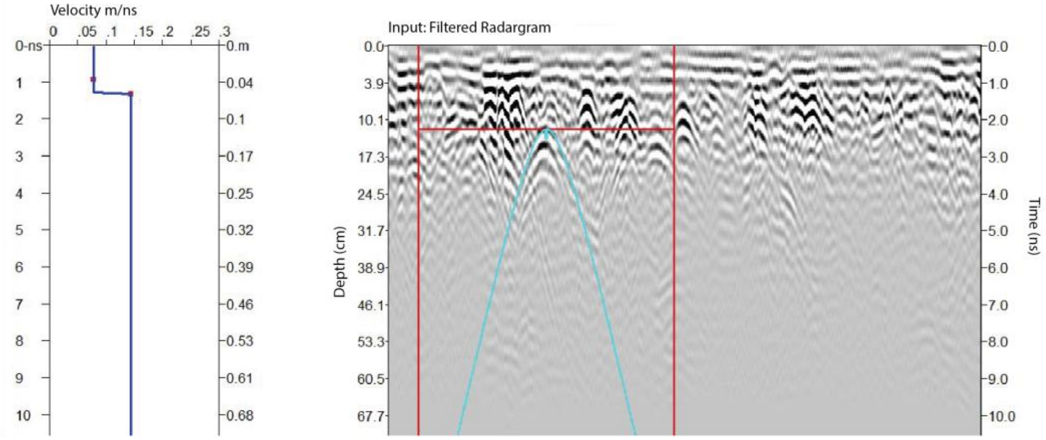

Figure 3.3: Unmigrated radargram and velocity profile obtained by fitting of diffraction curves. Note increase in velocity below x ns due to changes in shallow soil moisture content and composition. Average soil column velocity of 1.133 m/ns was employed in depth conversion of radagrams.

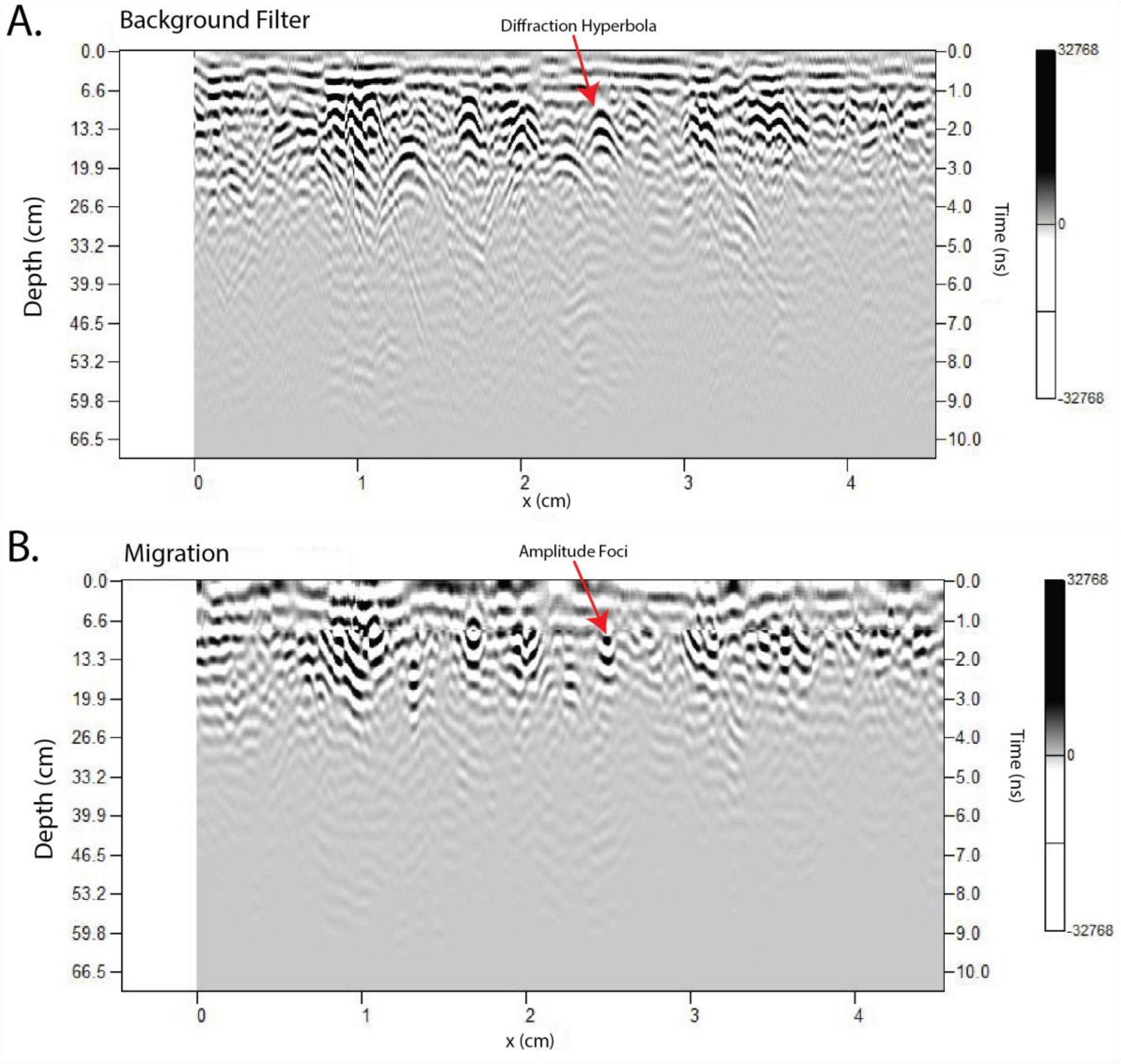

Figure 3.4: (A) Unmigrated profile showing multiple root diffraction events. (B) 2-D Kirchoff migrated Radargram with 2-D (Kirchoff) migration applied with block velocity model. Note diffractions collapse to well-defined amplitude foci.

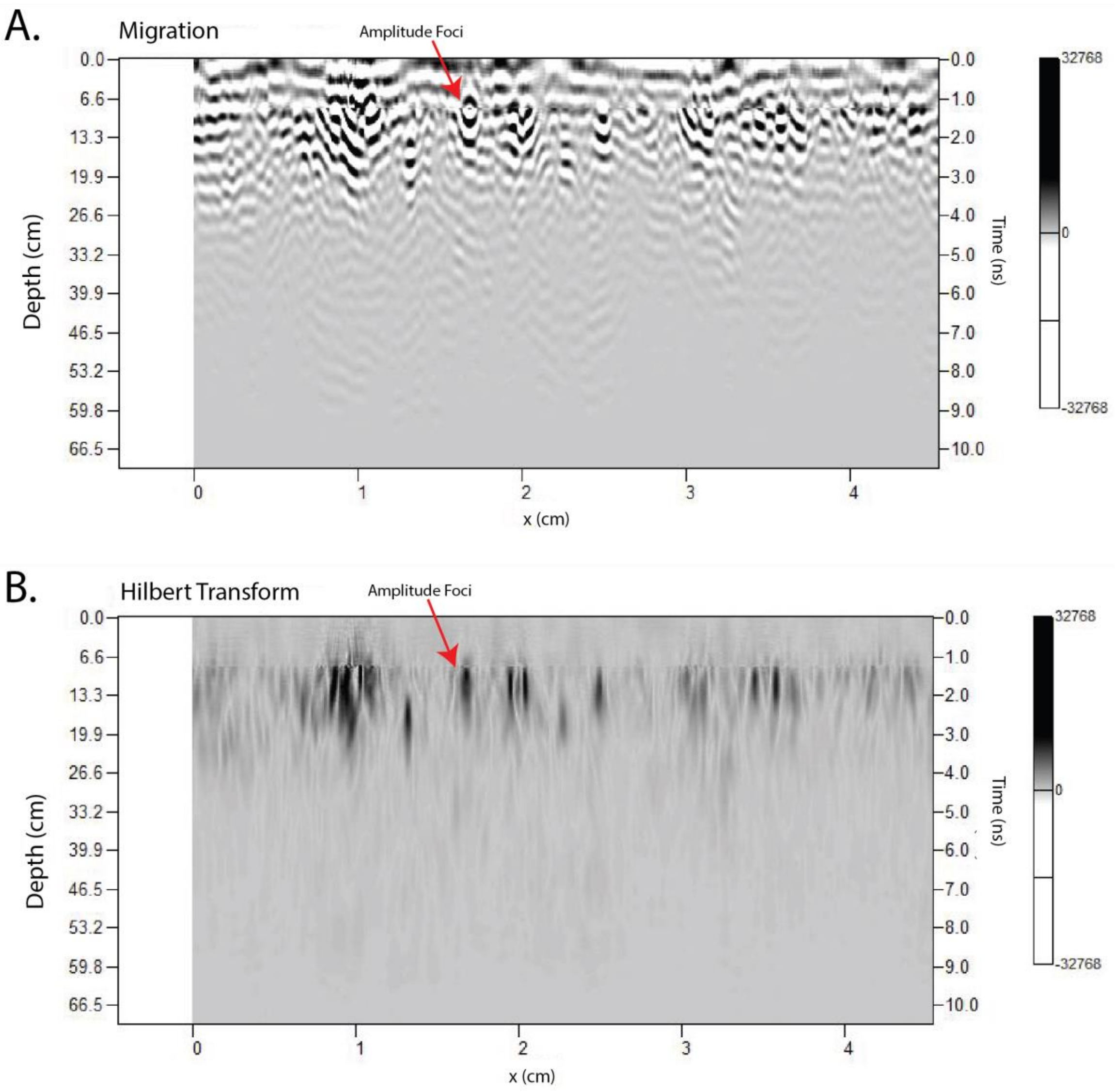

Figure 3.5: (A) Migrated radargram. (B) Hilbert-transformed radargram.

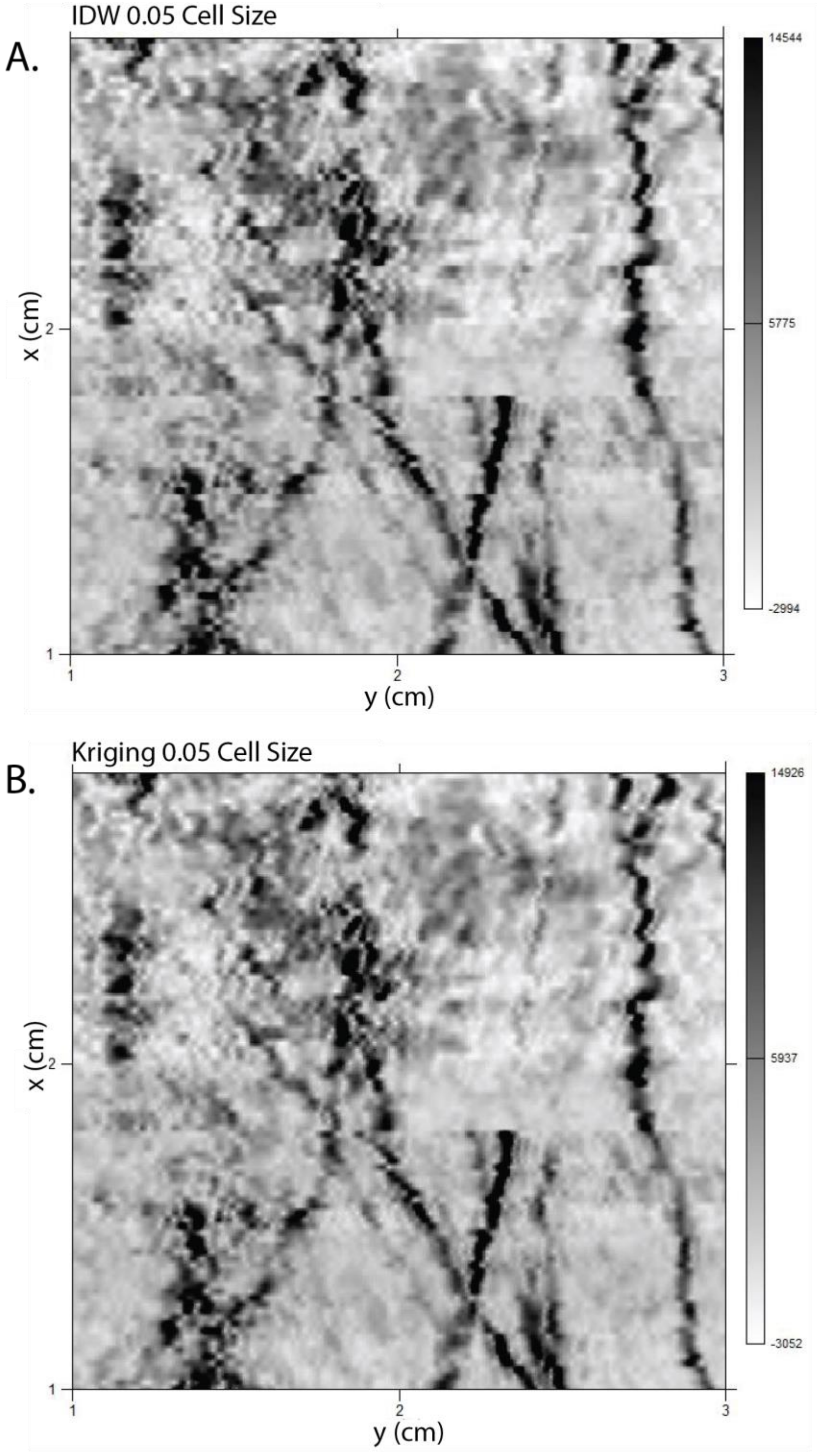

Figure 3.6: Comparison of IDW (A) and Kriging (B) interpolation of the 4-m2 subset area (20 cm depth). Grids produced with identical parameters (grid cell = 0.01 m, r = 0.05 m). The two grids appear nearly identical but computational efficiency of IDW is about 20 times that of Kriging.

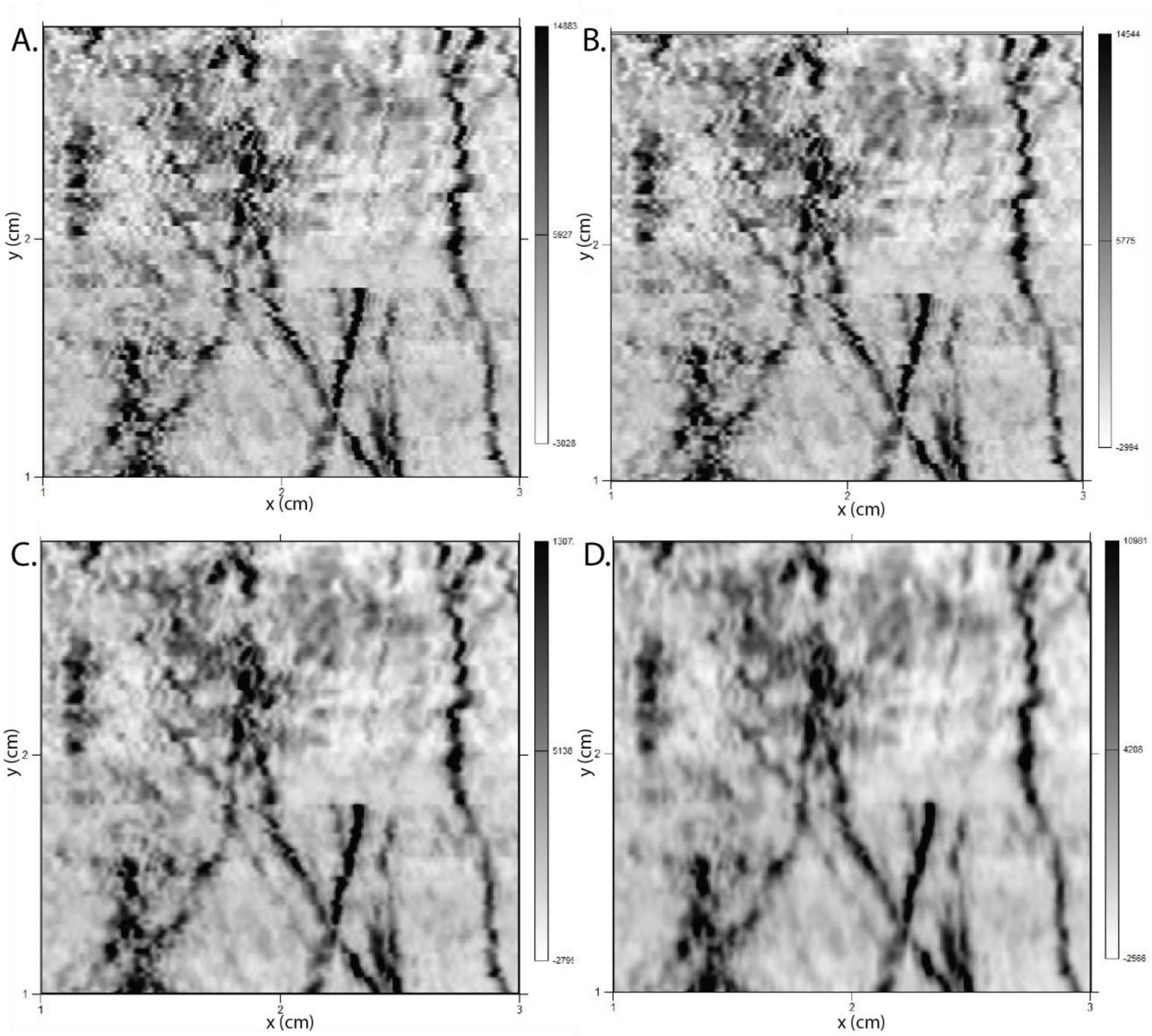

Figure 3.7: Time slices (20 cm depth) gridded using differing search radii. (A) r = 0.01, (B) r = 0.02, (C) r = 0.05, and (D) r = 0.1. Note the improving coherency as the search radii increases.

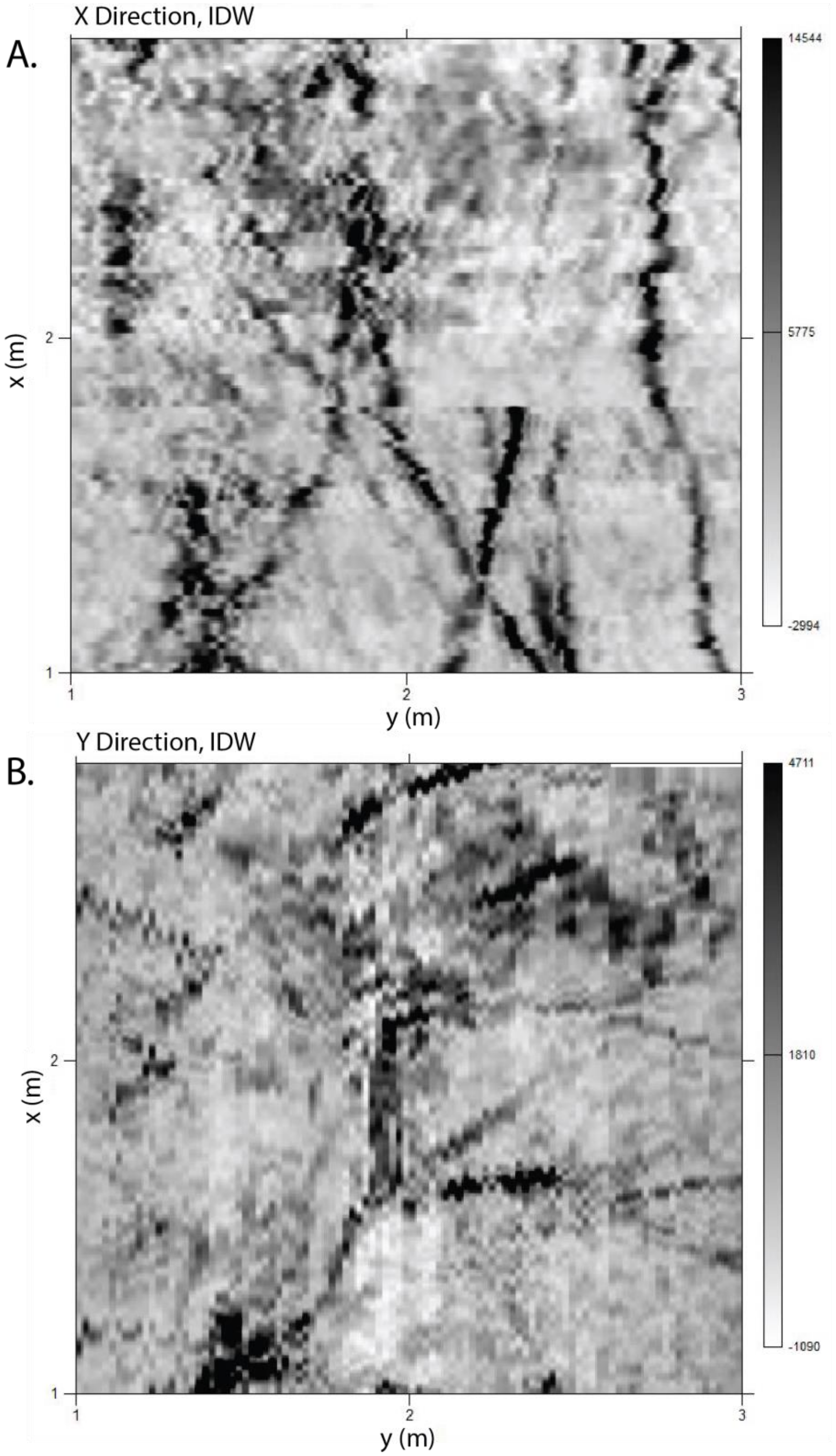

Figure 3.8: Time slices at 20 cm depth for 4-m2 subset area for (A) X-line and (B) Y-line directions. Both slices were gridded with the same parameters; X search radius of 0.1, Y search radius of 0.02, a blanking radius of 0.06, and an inverse distance weight of 2.

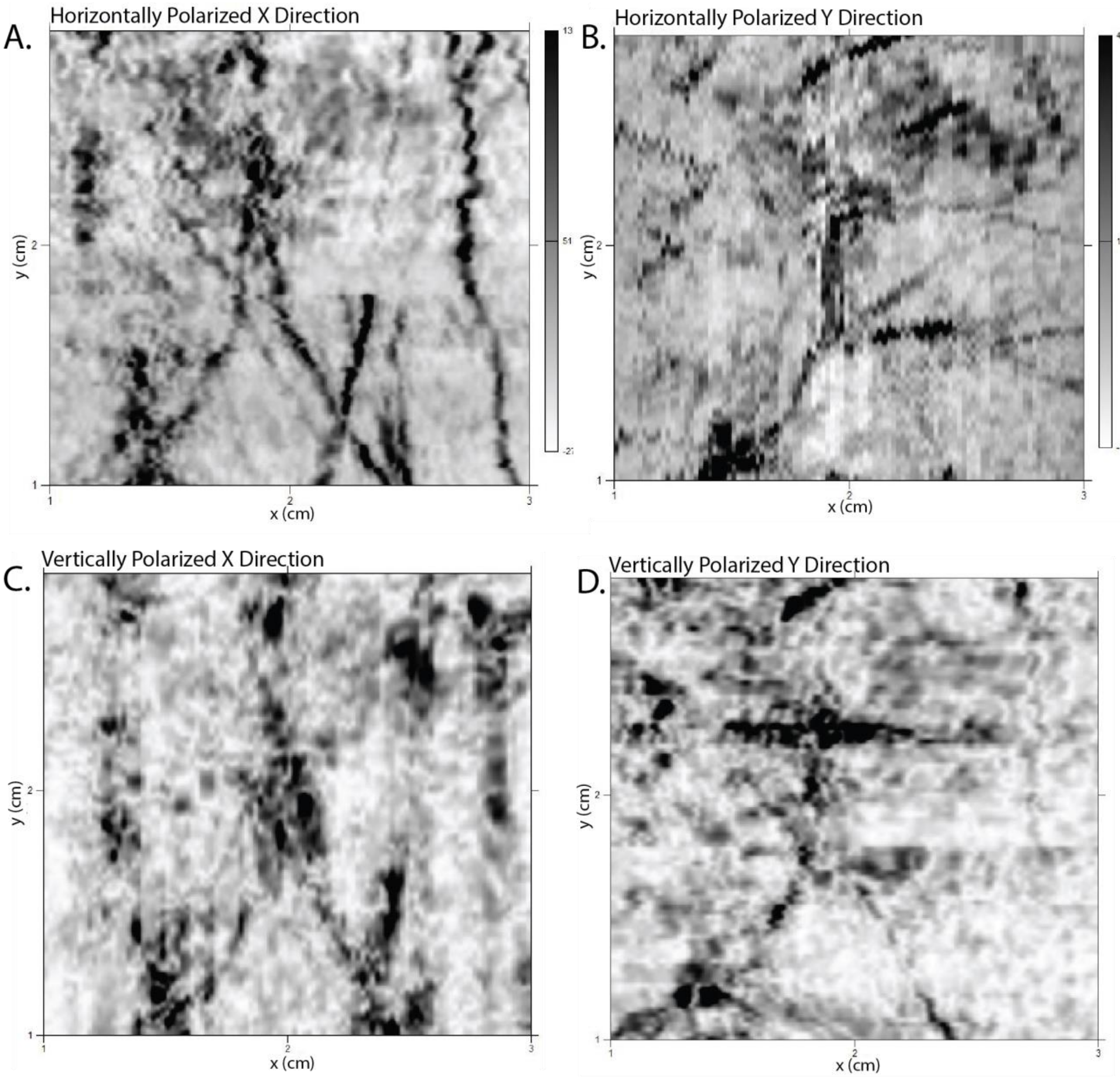

Figure 3.9: Comparison of depth slices for HH and VV antenna polarization for subset 4-m2 area. (A) HH X-lines (B) HH Y-lines, (C) VV and Y (D) directions. All four depth slices were gridded using the same parameters (X search radius of 0.01, Y search radius of 0.02, blanking radius of 0.06, and an inverse distance weight of 2).

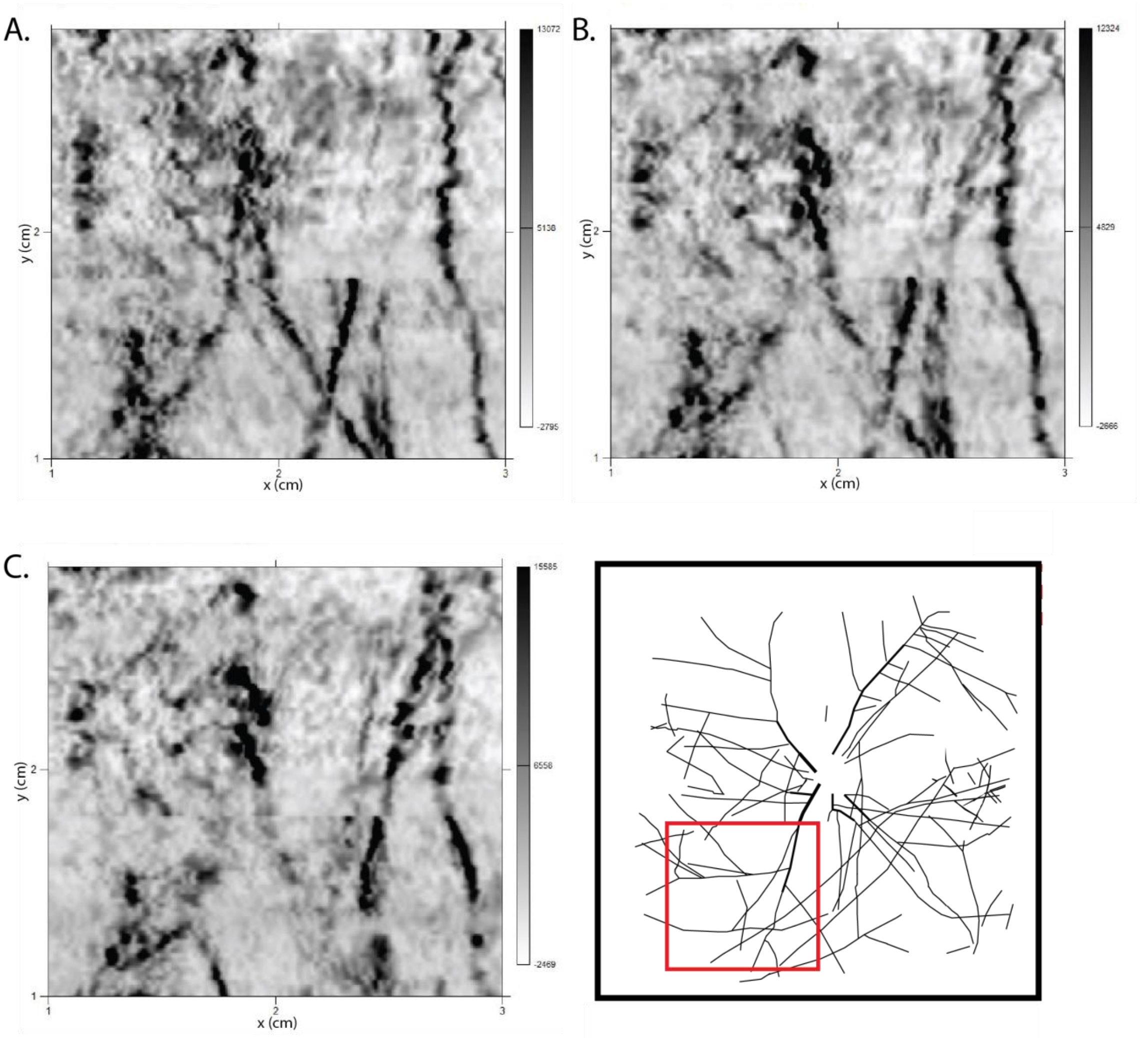

Figure 3.10: R4HH depth slices at (A) 11 cm (B), 13 cm and (C) 16 cm (C). (D) A Vectorized image of the excavated root network. The red square signifies the same area that the depth slices represent.

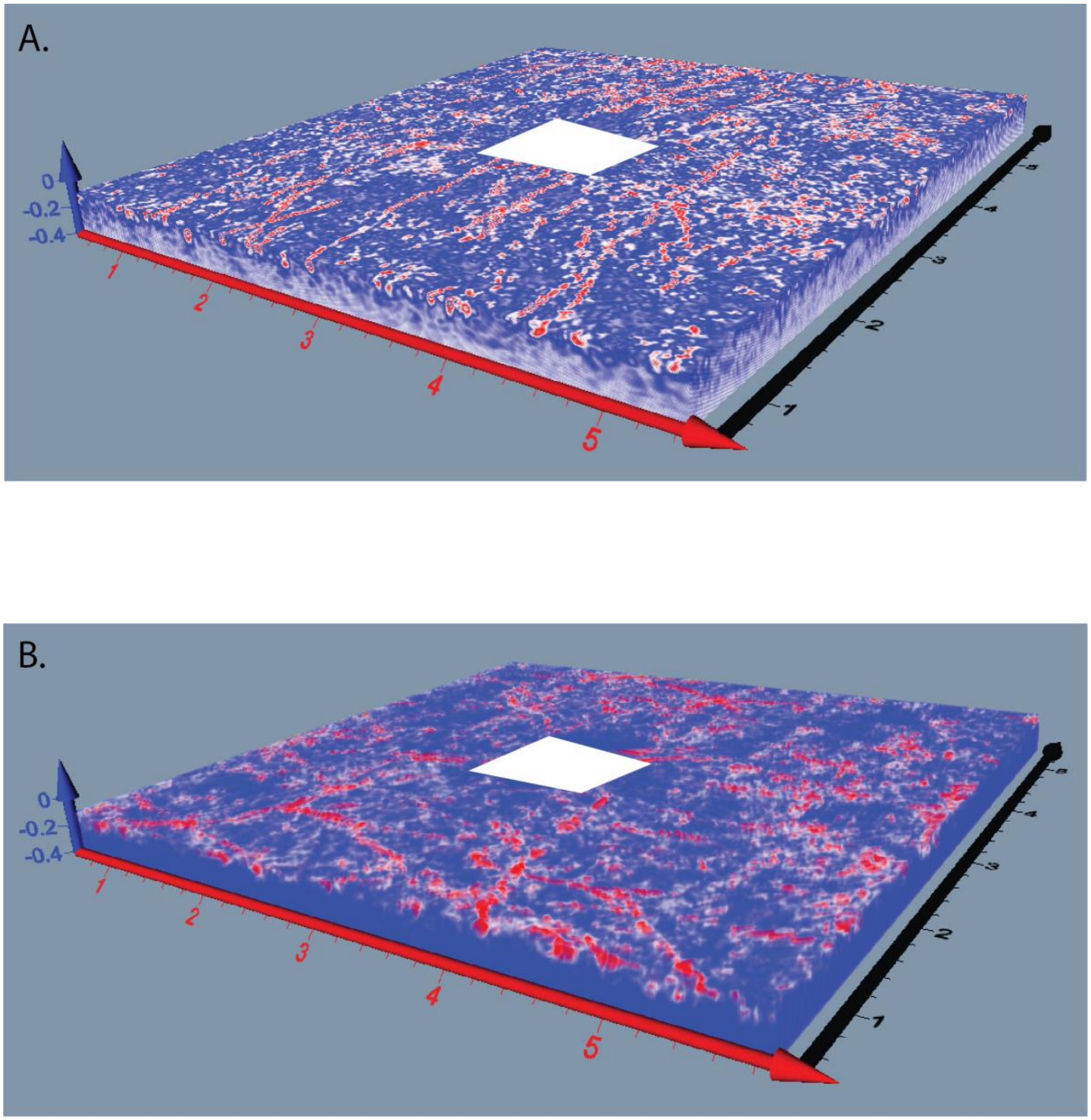

Figure 3.11: Interpolated 3-D radar volumes: (A) R4HH X-lines (B) R4HH Y-lines.

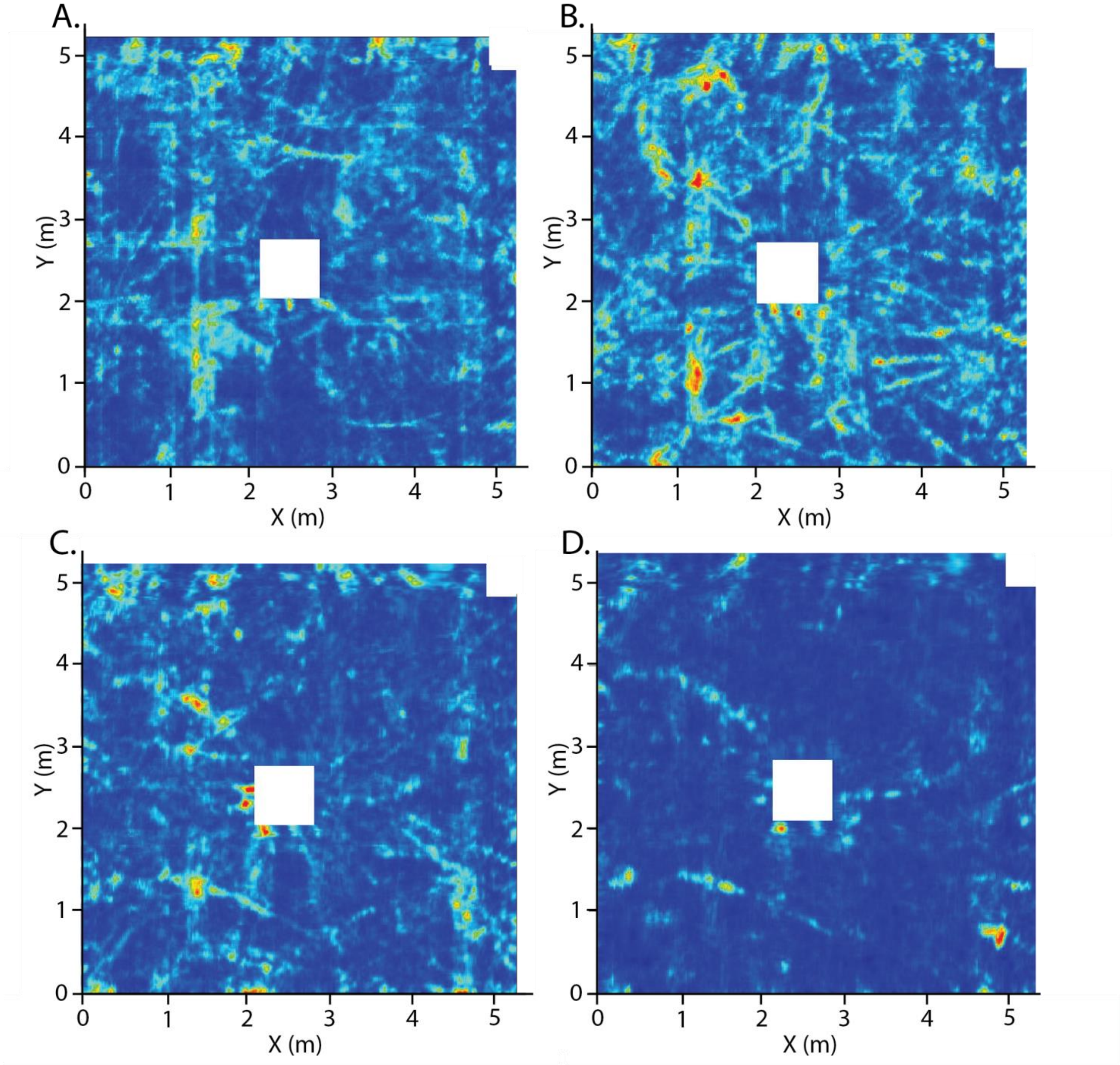

Figure 3.12: R4HH radar volume time slices. (A) 5 cm depth, (B) was taken at a depth of 10 cm, (C) was taken at a depth of 15 cm, and (D) 20 cm depth.

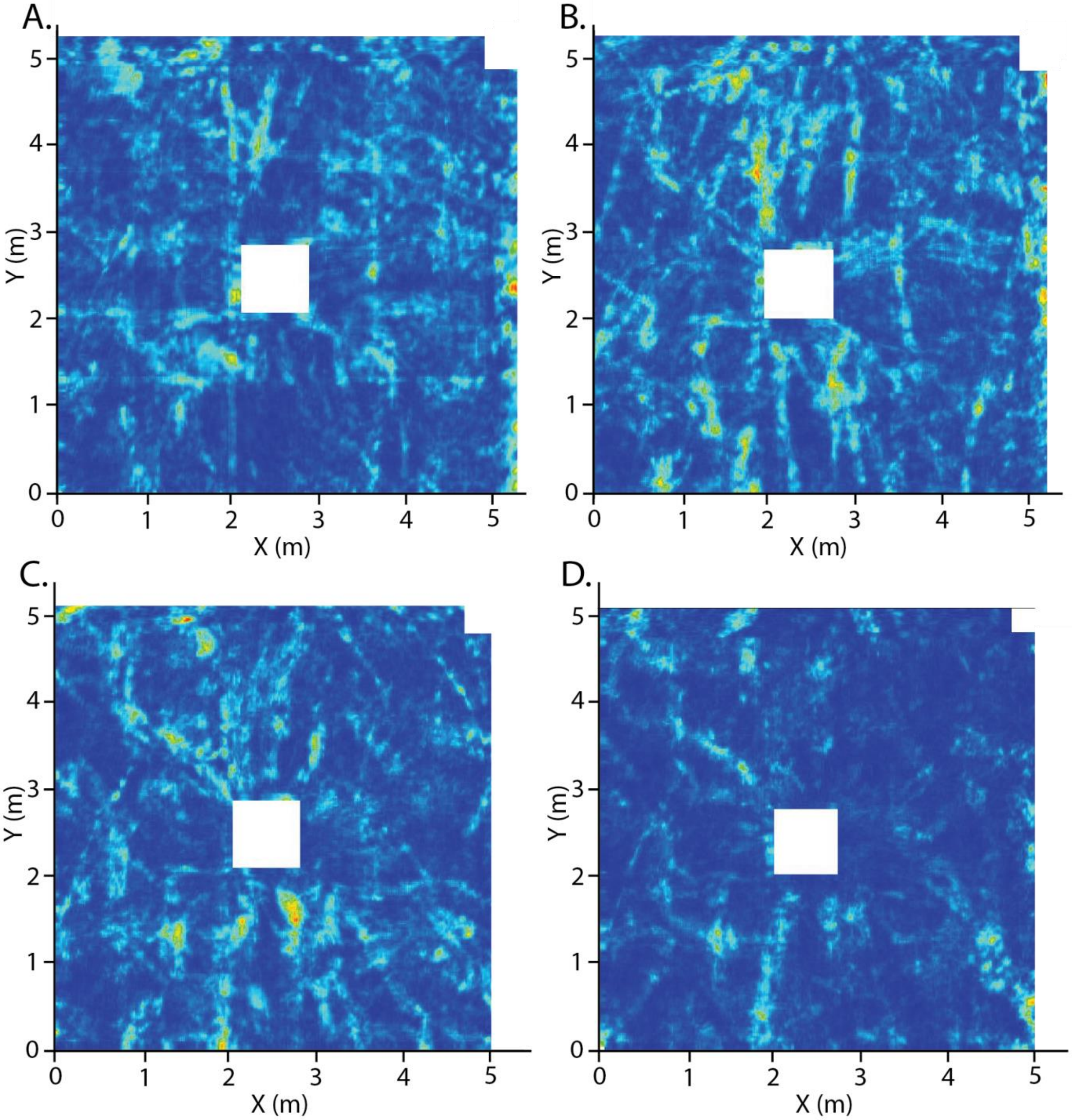

Figure 3.13: R4VV radar volume time slices. (A) 5 cm (B) 10 cm, (C) 15 cm, and (D) 20 cm depth.

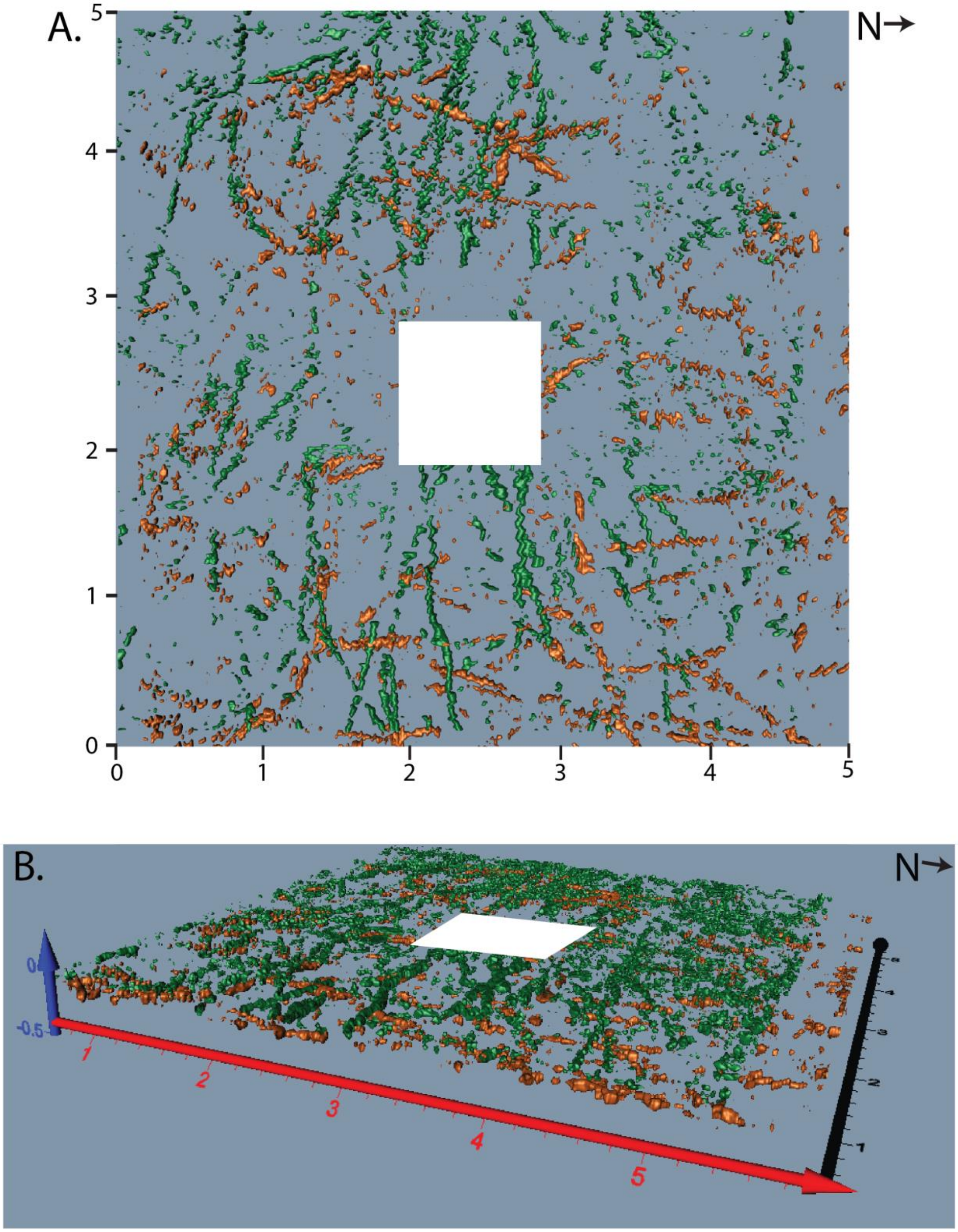

Figure 3.14: Isosurface volume of R4HH. (A) plan view, (B) and a 3-D view. The orange represents the data recorded in the Y direction and the green represents the data recorded in the X direction.

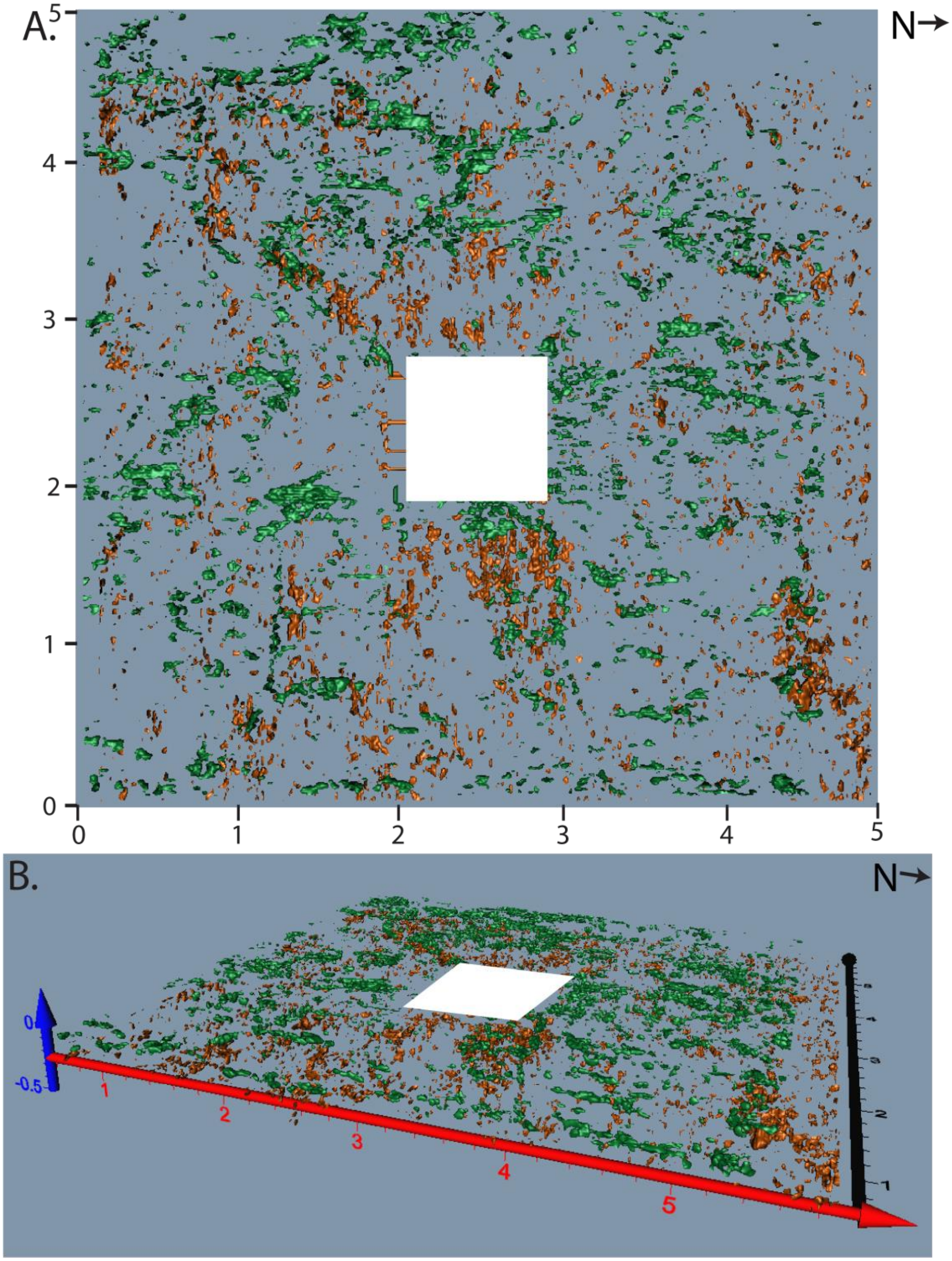

Figure 3.15: Isosurface volume of R4VV. (A) plan view, (B) 3-D view (B). The orange represents the data recorded in the Y direction and the green represents the data recorded in the X direction.

Chapter 4: Discussion

4.1 Root Detection and GPR Resolution

The vertical and horizontal GPR resolutions were evaluated by comparing GPR depth slices and Hilbert radargrams for the 4-m^2 subset area (Fig. 2.2). The 2-GHz transmit pulse was able to penetrate to a depth around 100 cm but the majority of the roots were found in the zone above 40 cm. Due to navigation and other errors the maximum resolution that could be achieved was more limited than expected; roots with diameter of 0.5 cm could be detected locally, but were not imaged as continuous root structures. The 2-GHz frequency permitted mapping of coarse roots (> 1-1.5 cm) and was able to map the very coarse (>3-5 cm) root network. The root zone of the juvenile white pine tree at the test site was quite shallow (10-40 cm), and most roots were concentrated in the depth range 10-15 cm. The 2-GHz frequency was effective for penetration at this depth but attenuation losses were significant below 50 cm depth. For other tree species and mature trees with rooting zones that extend below 50 cm depth, the 2-GHz system might not be effective and 1-GHz system may be required. The reduction in centre frequency would associate a reduction in vertical and horizontal resolution.

Areas of closely-spaced and overlapping roots produced very strong reflections and complex diffraction patterns (Fig. 3.5), which limited the detection of individual roots. In addition, the larger roots produce much higher amplitude reflections, which limited the transmission of the radar pulse preventing imaging of roots at greater depths. There are also a number of locations in the survey site where small roots intersected with much larger roots causing only the larger root to be detected or causing the two roots merge together as a single diffraction event.

Comparison of the GPR depth slices (Figs. 3.12, 3.13) with the actual root network indicates that the many roots were not detected, or some roots have different orientation than mapped by GPR. It was noted during air-spading some roots were disturbed and displaced from their growth location. For example, many thin < 1 cm roots in the shallow (10-15 cm) upper part of the soil column dropped to the base of the excavation when the soil support was removed. The root disturbance may account for apparent errors in root locations in GPR. A further factor, is distortion in vectorized root network (Fig. 2.2) produced by parallax in the overhead photo. The photo was not taken from directly overhead which leads to a distortion in the location of roots in the plan orthorectified image. This could account for errors in positioning of the root system in the vector root map versus the GPR depth slices. Future work could employ a digital SLR camera mounted on boom and gimbal system to allow direct overhead mapping of the root network.

GPR root reflectance is strongly controlled by the soil moisture content and the relative permittivity contrast between the roots and surrounding soil medium. The ideal dry sandy soil conditions during the test period were a critical factor in ensuring maximum detection rate of roots. Small variations in soil moisture content, particularly in the upper organic layer (A-horizon, 1-5 cm) may have contributed to the variable detection rate of roots at the site. Below the organic layer, the soil B horizon was a well-sorted sandy luvisol consisting of primarily of sand-sized particles (98%) and very few pebbles. This soil composition was very uniform environment for GPR work. The uppermost leaf litter layer (O-horizon) was removed prior to survey and was not a factor variable root detection.

The 3-D isosurface images of the white pine root network are the most detailed GPR images of a tree root system collected to date. Most previous work has emphasized the use of 2-D profiles (B-scans) and time slices (C-scans) for mapping tree root architecture (Butnor et al., 2001, 2004; Borden et al., 2015).

Full-resolution 3-D imaging of root networks has been very limited, due to the more intensive processing and computational requirements.

The detail in both resolution and coherency of this collected data is much better than that presented by both Novo et al. (2008) and Grasmueck and Novo (2016). Grasmueck and Novo performed a large 250m^2 survey in an attempt to detect multiple types of objects using a 500 MHz single channel antenna. While Grasmueck and Novo surveyed a 250m^2 area, they performed smaller 7 x 7 m surveys with spacing line spacing of 50 cm within the area. Though tree roots were imaged, the smallest diameter root that was found was only 2.5 cm, which is just over five times as large as the smallest root found in this study (Grasmueck and Novo, 2016). The time slices, 3-D volumes, and isosurfaces generated in this study are of a higher resolution due to the smaller line spacing and X and Y direction data collection.

As anticipated, the root detection was strongly dependent on the root orientation (Tanikawa et al., 2015). Both X and Y isosurface were able to identify coarse roots but smaller roots were not well imaged in isosurfaces compared with the gridded volumes. The X direction volumes were similar to the Y direction volumes; providing a clear image with roots that were perpendicular to the survey direction (Fig. 3.9). Overall, the horizontally polarized (HH) antennas provided the clearest and most accurate root network images (Fig. 3.12 vs. Fig. 3.13).

4.2 GPR Polarization

Roots were detected in both the HH and VV mode radargrams, however, the horizontally-polarized dataset provided a much clearer and more coherent image of the root network. This was true for both the X- and Y-line directions. Though the vertically polarized (VV) data imaged some coarse roots, the root detection rate was much lower and roots were resolved with much less detail (Figure 3.9). The superior detection of roots by the HH mode antenna array relates to the orientation of the electric field vector. Roots can be considered as linear targets with moderate impedance, which couple more strongly with the radar wave when the electrical vector E_v is parallel to the root structure (Radezvicius et al., 2000).

4.3 Biomass Estimation

A number of recent studies have employed GPR for quantitative root biomass estimation (Guo et al., 2013) but few studies have attempted to extract biomass values from 3-D radar volumes. Most studies have estimated biomass using regression of measured root diameter on various indices derived from 2-D radargrams (B-scans) or GPR time slices (C-scans). For example, Borden et al. (2014) performed a 4.5 x 4.5 m grid survey on five different species of trees with 10 cm line spacing using a 1- GHz GPR system. They determined a mean root biomass of 54.1 ± 8.7 kg tree^{-1} using regressed measured root diameter and amplitude index area. Raz-Yaseef et al. (2013) utilized a 1-GHz GPR to survey seven 8 x 8 m grids with a line spacing of 20 cm. They were able to detect roots as small as 13 mm, roughly double the diameter detected in this study. The estimated average root biomass for their site was 3.5± 1.4 kgCm^{-2}. Both of these studies utilized 1-GHz antennas and larger line spacing, which limited the detection of finer roots. More recently, Molon et al., (2017) estimated root biomass over a 400-m^2 area of white pine forest with a single-channel 1-GHz GPR. Unlike previous studies which employed statistical relationships between root diameter and reflection amplitude or waveform indices, they modelled roots using isosurface volumes calculated on Hilbert transformed 3-D volume. The root biomass (0.92 kgCm^{-2}) was estimated by summing the voxels within root isosurface and calibrated against a set of roots reburied in an experimental test pit. The 3-D GPR volume in that study was acquired with line separations of 5-25 cm, which did not meet the Nyquist quarter wavelength for full-resolution 3-D imaging. As a result, many roots were not imaged completely, and the biomass calculation produced a lower estimate than conventional allometric methods.

This study demonstrates that with full-resolution 3-D GPR imaging the coarse root network can mapped for roots >3 cm. Estimates of the coarse root volume and belowground carbon could be obtained using the methods developed by Molon et al. (2017). Quantitative estimates would require calibration of the GPR isosurface threshold amplitude, which was not conducted as part of this study. As simple test of the method, the isosurface volumes of the root networks in Figures 3.14 and 3.15 were calculated in Voxler 4. The tree root volume for R4HH was 0.277 m^3 and for and R4VV, 0.464 m^3. This volume is an approximation of the root volume of the detected roots but is likely an underestimation of the total root volume for the tree as many coarse roots were undetected due to incomplete imaging of unfavourable oriented roots, and fine roots less than 1 cm, which cannot be detected. Despite this shortcoming, the isosurface volume calculation provides an method for obtaining a first order approximation of the biomass of large roots.

Estimation of the absolute biomass using GPR will likely lead to an underestimation of the total root biomass. However, the method can be utilized to monitor annual changes in biomass by conducting repeat surveys (identical parameters and equipment) at the same location in order to measure the growth of the roots. The first survey would act as a baseline value with subsequent surveys having their totals subtracted to calculate the change in root biomass over time. This method would ideally be used on a bi-annual or annual basis. As afforestation is becoming more prevalent in countries around the world to draw down carbon dioxide levels, approach could provide a tool to measure change in carbon over time in root networks.

Chapter 5: Summary and Conclusions

This study evaluated the ability of a 2-GHz multichannel GPR for detecting and mapping a white pine tree root network. The 3-D GPR survey was conducted on a 25-m^2 test plot with 2-cm line spacing under near ideal, dry sandy soil conditions. After the survey was completed, the root network was excavated and photographed for comparison with the 3-D root architecture mapped in depth slices and isosurface models (Figs. 3.10-3.15). The primary conclusions of the study are as follows:

1) the 2-GHz multi-channel GPR system was able to successfully image the coarse root network of a juvenile white pine, utilizing a 16-channel multichannel antenna array with dual polarized arrays.

2) Roots as small as 0.5 cm were detected with the 2-GHz frequency, but many roots <1.5 cm diameter could not be detected as continuous root structures,

3) The orientation of roots strongly controlled root detection; roots oriented at >30-45 degrees to the survey swaths were imaged incompletely or not detected.

4) Most large coarse roots (>5 cm diameter) were mapped as continuous structures when the root orientation was either parallel to, or perpendicular to the GPR transects.

5) The highest rate of root detection was achieved using horizontally polarized antenna array (HH) and vertical polarization (VV) was not effective,

6) Isosurface root models constructed from the Hilbert-transformed radargrams allowed mapping of the 3-D root architecture for large (> 3-5 cm diameter) roots and could provide a means for quantifying root volume and biomass in future work.

5.1 Future Work

There are several improvements that could be made to the field methods to improve the GPR data quality and root detection. As identified in Chapter 3, navigation errors resulting from odometer wheel slippage were the most significant source of error in the inline positioning of radargrams. The wheel slippage resulted in mispositioning of GPR traces, causing a 'zig-zag' staggered pattern in the interpolated depth slices. These offsets reduced the coherency of the interpolated 3-D radar volumes in many areas of the survey grid. Increasing the interpolation radius was effective in smoothing small offsets but resulted in severe smearing where the trace offsets were greater than 1-2 cm. In order to minimize these navigational errors it is recommended in future work that a laser theodolite or real-time kinematic (RTK) D-GPS positioning system is used in combination with the guide rail. Modern robotic laser theodolite systems are capable of achieving sub-centimetric and millimetric positioning, and can also provide pitch, roll and yaw angles for correction platform motion (e.g. Molon, 2012). These methods will allow for high-precision GPR positioning and would significantly enhance the final resolution in 3-D volumes and depth slices.

A further source of positional error was the design of the guide rail system. The guide rail was fabricated from wooden 2 x 4-inch lumber and supported at both ends by perimeter box and at its centre by a small wooden support. At the centermost point the guide rail may have not been able to maintain full rigidity which could have caused a slight veering off course increasing or decreasing the overall length of the lines in question. In order to eliminate this it would be wise to have the guide rail be supported in numerous locations, or to have it on wheels and rest on the aforementioned flat surface.

A second problem encountered was the surface microtopography at the survey test sites. The Hi-BrigHT multichannel antenna was designed for primarily for survey of smooth man-made surface (e.g. concrete, asphalt). Due to the large antenna footprint and area, small irregularities in the forest floor topography caused a partial 'lift-off' of the antenna, causing if to decouple from the ground surface. The decoupling produced air wave reflections from the ground surface, which in turn introduced significant large amplitude noise in the early part of the radargrams. These noise effects were successfully suppressed by a combination of background and bandpass filtering of the data, but in some radargrams the noise contamination affected imaging of shallow roots in the upper 20 cm of the soil profile. In the future, airwave noise effects could be minimized by careful levelling of the sand surface of the survey site to ensure it is as flat as possible. The sandy surface also produced issues with survey wheel slippage; this could be prevented by spreading of a heavy-duty plastic tarp across the survey site to provide grip for the survey wheel.

The orthogonal survey grid employed in this study was the most efficient way to acquire a full-resolution swath coverage at 2-cm line spacing using a guide rail system. Due to the dependency of root detection on root orientation the data quality and root detection rate could be improved using a radial survey approach (e.g. Hickson, 2016). In a radial survey lines are acquired in a circular pattern around the tree, which produces a large number of 90° root crossings due to the radial pattern of tree roots. Performing a radial survey in addition to the XY grid that was completed could have yielded important information regarding the position of roots at 45 degrees to the XY grid. A radial survey would also have allowed for a more precise location of some of the larger angled roots as seen in Figure 2.2.

Imaging of roots could be improved by varying the swath direction within the grid to maximize perpendicular root crossings. In this approach, the lines would be collected as perpendicular X and Y swath sets as in this study, and then two additional swaths sets acquired at 45° angle to the X and Y baselines to provide a very high sampling density. This approach would maximize root detection but would be highly labour intensive, as moving the Hi-BrigHT antenna in a radial pattern would prove difficult due to its size and maneuverability. Radial surveys even with a single-channel 1-GHz monostatic antenna can be a challenge to collect (Hickson, 2016). The survey positioning requirements are also more challenging when collecting circular profiles, and require the use of either high-precision kinematic D-GPS or laser theodolite to track the antenna locations.

Future work at the TP74 test site will include testing of radial survey methods using laser theodolite positioning system to improve the navigation precision. 3-D GPR surveys will also continue at the second test site (TP74-J; Juliet) to evaluate long-term GPR monitoring of temporal changes in root biomass. 3-D GPR volumes will be acquired annually over a 5-year period and the change in biomass determined by subtraction of the isosurface volumes. This approach will also allow monitoring of tree growth in relation changes in climate and environmental variables at TP74.

Root mapping and underground biomass estimation is a relatively new and rapidly developing application of GPR (Guo et al., 2013; Molon et al., 2017). The advent of multi-channel GPR systems has been an important technological development, allowing increased GPR survey efficiency and improved 3-D image resolution and target detection (e.g. Grasmueck and Novo, 2016). Future improvement in both the field data acquisition methods, survey design and data processing will likely expand the application of 3-D multi-channel GPR in root studies and will lead to new improved approaches for quantitative estimation of belowground biomass.

References

Al Hagrey, S. A. (2007) Geophysical imaging of root-zone, trunk, and moisture heterogeneity. J. Exp. Bot., 58, 839-854.

Annan, A.P., 2003. Ground Penetrating Radar Principles, Procedures & Applications. Sensors & Software, Inc., Mississauga, Ontario, Canada. 278 p.

Annan, A.P. and Cosway, S.W. (1992) Ground penetrating radar design: Proceedings of the Symposium on the Applications of Geophysics to Engineering and Environmental Problems, April 26-29, 1992, Oakbrook, IL, p. 329-351.

Arain, A. and Restrepo-Coupe, N. (2005) Net ecosystem production in a temperate pine plantation in southeastern Canada. *Agricultural and Forest Meteorology*, 128, 223-241.

Baker, G., Jordan, T., and Pardy, J. (2007) AN introduction to ground penetrating radar. Geological Society of America Special Paper 432, 1-18.

Barton, C., and Montagu, K. (2004) Detection of tree roots and determination of root diameters by ground penetrating radar under optimal conditions. *Tree Physiology*, 24, 1323-1331.

Bassuk, N., Grabosky, J., Mucciardi, A., and Raffel, G. (2011). Ground-penetrating Radar Accurately Locates Tree Roots in Two Soil Media Under Pavement. *Arboriculture & Urban Forestry*, 37, 160-166.

Borden, K., Isaac, M., Thevathasan, N., Gordon, A., and Thomas, S. (2014) Estimating coarse root biomass with ground penetrating radar in a tree-based intercropping system. Agroforest Syst. DOI 10.1007/s10457-014-9722-5.

Butnor, J., Doolittle, K., Hognsen, K., Samuelson, T., Stokes, T., and Kess, L. (2003) Utility of ground penetrating radar as a root biomass survey tool in forest systems. Soil *Science Society of America*, 67, 1607-1615.

Butnor, J., Roth, B., and Johnsen, J. (2005) Feasibility of using ground-penetrating radar to quantify root mass in Florida's intensively managed pine plantations. Forest Biology Research Cooperative Report Number 28, University of Florida, Gainsville, Florida.

Butnor, K., Barton, C., Day, F., Shoeder, R., Johnsen, K., Mucciardi, A., and Stover, D. (2012) Using ground-penetrating radar to detect tree roots and estimate biomass, in Measuring Roots, edited by S. Mancuso, 213-245, Springer, Berlin.

Cassidy, N. J. (2009). Ground penetrating radar data processing, modelling and analysis. *Ground penetrating radar: theory and applications*, 141-176.

Cassidy, N.J., and Millington, T.M. (2009) The application of finite-difference time-domain modelling for the assessment of GPR in magnetically lossy materials. *Journal of Applied Geophysics*, 67, 296-308.

Conyers, L., and Goodman, D. (1997) Ground-Penetrating Radar: An Introduction for Archaeologists, pp. 232. AltaMira Press.

Conyers, B. (2004) Moisture and Soil Differences as Related to the Spatial Accuracy of GPR Amplitude Maps at Two Archaeological Test Sites.

Cox, K. D., Scherm, H., and Serman, N. (2005) Ground-penetrating Radar to Detect and Quantify Residual Root Fragments Following Peach Orchard Clearing. *HortTechnology*, 15, 600-607.

Cui, X., Chen, J., JinSong, S., Cao, K., Chen, X., and Zhu, X. (2011) Modelling tree root diameter and biomass by ground penetrating radar. *Science China Earth Sciences*, 54, 711-719.

Cui, X., Guo, L., Chen, J., Chen, X., and Zhu, X. (2013) Estimating tree-root biomass in different depths using ground-penetrating radar: evidence from a controlled experiment. *IEEE Transactions on Geoscience and Remote Sensing*, 51, 3410-3423.

Dannoura, M., Hirano, Y., Igarashi, T., Ishii, M., Aono, K., Yamase, K and Kanazawa, Y. (2008) Detection of *Crptomeria japonica* roots with ground penetrating radar. Plant Biosystems., 142, 375-380.

Dixon, R., Brown, S., Houghton, R., Solomon, A., Trexler, M., and Wisniewski, J. (1994) Carbon pools and Flux of Global Forest Ecosystems. Science., 263, 185-191.

Fisher, E., McMechan, G.A., and Annan, A. P. (1992) Acquisition and processing of wide-aperture ground-penetrating radar data. *Geophysics*, 57, 495-504.

Goodman, D. (2016) GPR-Slice v7 User's Manual, pp. 15-270, Geophysical Archaeometry Laboratory Inc., Woodland Hills, California, USA.

Goodman , D. and Piro, S. (2013) GPR Remote Sensing in Archaeology. Ney York, United States: Springer.

Gormally, K., McIntosh, M., and Mucciardi, A. (2011) Ground-Penetrating Radar Detection and Three-Dimensional Mapping of Lateral Macropores: I. Calibration. *Soil Sci. Soc. Am. J*. 75, 1226-1235.

Grasmueck, M., Weger, R., and Horstmeyer, H. (2005) Full Resolution 3D GPR imaging. *Geophysics*, 70, 12-19.

Grasmueck, M., and Viggiano, D.A. (2007) Integration of Ground-Penetrating Radar and Laser Position Sensors for Real-Time 3-D Data Fusion. *IEEE Transactions on Geoscience and Remote Sensing*, 45, 130-137.

Grasmueck, M., and Novo, A. (2016) 3D GPR Imaging of Shallow Plastic Pipes, Tree Roots, and Small Objects. *2016 16th International Conference of Ground Penetrating Radar (GPR).*

Guo, L., Chen, J., Cui, X., Fan, B., and Lin, H. (2013) Application of ground penetrating radar for coarse root detection and quantification: a review. *Plant Soil*, 362, 1-23.

Hirano, Y., Dannoura, M., Aono, K., Igarashi, T., Ishii, M., Yamase, K., Makita, N., and Kanazawa, Y. (2009) Limiting factors in the detection of tree roots using ground-penetrating radar. *Plant Soil*, 319, 15-24.

Hirano, Y., Dannoura, M., Aono, K., Igarashi, T., Ishii, M., Yamase, K., Makita, N., and Kanazawa, Y. (2012) Detection frequency of *Pinus thunbergii* roots by ground-penetrating radar is related to root biomass. *Plant Soil*, 360, 363-373.

Hruska, J., Cemak, J, and Sustek., S. (1999) Mapping tree root systems with ground penetrating radar. Tree Physiology, 19, 125-130.

Huisman, J. A., Hubbard, S. S., Redman, J. D., and Annan, A. P. (2003) Measuring Soil Water Content with Ground Penetrating Radar: A Review. *Soil Science Society of America*, 2, 476-491.

Isaac, M., Anglaaere, L. (2013) An insitu approach to detect tree root ecology: linking ground-penetrating radar imaging to isotope-derived water acquisition zones. *Ecology and Evolution*, 3(5), 1330-1339.

Jol, H.M., and Bristow, C.S., 2003, GPR in sediments: Advice on data collection, basic processing and interpretation, a good practice guide, in Bristow, C.S., and Jol, H.M., eds., Ground Penetrating Radar in Sediments: Geological Society [London] Special Publication 211, p. 9–27.

Kim, J. H., Cho, S. J., & Yi, M. J. (2007). Removal of ringing noise in GPR data by signal processing. *Geosciences Journal*, *11*(1), 75-81.

Liu, L., & Oristaglio, M. (1998). GPR signal analysis: instantaneous parameter estimation using the wavelet transform. *GPR Proceedings , 1*, 219-224.

Lorensen, W. E., and Cline, H.E. (1987) Marching Cubes: A high resolution 3D surface construction algorithm. *Computer Graphics*, 21(4), 163-169.

Luo, Y., Al-Dossary, S., Marhoon, M. and Alfaraj, M., (2003) Generalized Hilbert transform and its applications in geophysics. *Leading Edge,* 22, 198, 200-202

Moran, M. L., Greenfield, R. J., Arcone, S. A., & Delaney, A. J. (2000). Multidimensional GPR array processing using Kirchhoff migration. *Journal of Applied Geophysics*, 43, 281-295.

Molon, M., Boyce, J., and Arain, A. (2017) Quantitative, non-destructive estimates of coarse rot biomass in a temperate pine forest using 3-D ground penetrating radar (GPR). *Journal of Geophysical Research*, 121.

Neal, A. (2004) Ground-penetrating radar and its use in sedimentology: principles, problems and progress. *Earth Science Reviews*., 66, 261-330.

Newman, T. S., and Yi, H. (2006) A survey of the marching cubes algorithm. *Computers and Graphics*, *30*, 854-879.

Peichl, M., and Arain, A. (2006) Above and belowground ecosystem biomass and carbon pools in an age-sequence of temperate pine plantation forests. *Agric. For. Meteorol.*, 140, 51-63.

Peichl, M., Arain, A., Ullah, S., and Moore, T. (2009) Carbon dioxide, methane, and nitrous oxide exchances in an age-sequence of temperate pine forests. *Global Chance Biol.*, 16, 2198-2212.

Peichl, M., Brodeur, J., Khomik, M., and Altaf, A. (2010a) Biometric and eddy-covariance based estimates of carbon fluxes in an age sequence of temperate pine forests. *Agriculture and Forest Meteorology*., 150, 952-965.

Radzevicius, S. J., & Daniels, J. J. (2000). Ground penetrating radar polarization and scattering from cylinders. *Journal of Applied Geophysics*, *45*, 111-125.

Raz-Yaseef, N., Koteen, L., and Baldocchi, D.D. (2013) Coarse root distribution of a semi-arid oak savanna estimated with ground penetrating radar. *Journal of Geophysical Research: Biogeosciences,* 118, 135-147. doi: 10.1029/2012JG002160.

Reynolds, J.M. (2011) An Introduction to Applied Environmental Geophysics: 2nd Edition. Oxford, United Kingdom: Wiley-Blackwell.

Rial, F. I., Pereira, M., Lorenzo, H., Arias, P., and Novo, A. (2009) Resolution of GPR bowtie antennas: An experimental approach. *Journal of Applied Geophysics*, 67, 367-373.

Simi, A., Guido, M., and Andra, B. Bridge deck survey with high resolution ground penetrating radar. (2012). 14th International Conference on Ground Penetrating Radar (GPR). 489-495

Stover, D., Day, F., Butnor, J., and Drake, B. (2007) Effect of elevated CO_2 on coarse root biomass in Florida scrub detected by ground penetrating radar. *Ecology*., 88, 1328-1334.

Tanikawa, T., Hirano, Y., Dannoura, M., Yamase, K., Aono, K., Ishii, M., Igarashi, T., Ikeno, H., and Kanazawa, Y. (2013) Root orientation can affect detection accuracy of ground penetrating radar. *Plant Soil*, 373, 317-327.

Wielopolski L., Hendrey G., McGuigan M., Daniels J.J. (2002) Imaging tree root systems in situ. Proceedings - 9th International Conference on GPR - SPIE - *International Society for Optical Engineering*, V4758, 58-62.

Wu, Y., Guo, L., Cui, X., Chen, J., Cao X., and Lin, H. (2013) Ground-penetrating radar-based automatic reconstruction of three-dimensional coarse root system architecture. *Plant Soil*, 383, 155-172.